Low Reynolds Number Airfoil Design Lecture Notes

Michael S. Selig*

Department of Aerospace Engineering
University of Illinois at Urbana–Champaign
Urbana, Illinois 61801 USA

VKI Lecture Series

Sponsored by
NATO Research and Technology Organization (RTO)
Applied Vehicle Technology (AVT) Panel
24–28 November 2003

Abstract

An approach to low Reynolds number airfoil design is described, and several example design cases are presented and discussed. The overall approach involves using the inverse method PROFOIL for design and XFOIL for analysis. Validation of these methods and the low Reynolds number airfoil design philosophy is supported by UIUC wind tunnel experiments. These notes derive largely from four prior publications of the author (see Refs. 1–4) and the contributions of the respective co-authors are gratefully acknowledged.

1 Introduction

For over 100 years, airfoil design has continued to capture the interest of practitioners of applied aerodynamics. The field is fueled by the ever-growing combination of airfoil design requirements for unique applications, such as UAVs, and this state of affairs is likely to continue. When one considers all possible permutations of the myriad of airfoil design requirements, it quickly becomes apparent that the number of unique sets of requirements far

*Associate Professor, 306 Talbot Laboratory, 104 S. Wright St. email: m-selig@uiuc.edu.

Presented at the von Karman Institute for Fluid Dynamics, Lecture Series: Low Reynolds Number Aerodynamics on Aircraft *including applications in* Emerging UAV Technology, 24–28 November 2003.

exceeds the collection of existing airfoils. For this reason, the advancement and use of methods for airfoil design continues to be the economical solution. In contrast, the enrichment of airfoil "catalogs" for their own sake is felt to be of limited value.

The objective of this lecture focuses on the design of airfoils for low Reynolds numbers, which has been the subject of considerable research as documented in several major conferences and books.[5–9] First, various approaches to airfoil design are discussed, leading to the use of inverse methods being favored over the alternatives. Second, several sections of these notes outline the important influence of laminar separation bubbles on low Reynolds number airfoils, leading to the need for an inverse method that has the unique capabilities of being able to more or less directly control the movement of transition with angle of attack. The desired behavior of transition forms the basis of a design philosophy that has been implemented in a methodology for inverse airfoil design. Finally, to illustrate the overall approach to low Reynolds number airfoil design, several example airfoils are presented in this lecture. In each case, state-of-the-art tools for airfoil design[10,11] and analysis[12–14] were used. Although these airfoils were each designed for specific applications, the systematic and parametric studies show useful performance trends and trade-offs in airfoil design at low Reynolds numbers. As will be shown, the overall design process has been validated through wind tunnel tests, and these results are presented together with the predictions.

2 Various Approaches to Airfoil Design

In this section, various approaches to airfoil design are briefly summarized. The alternative to our great legacy of airfoil design by geometric means guided by empirical study (Fig. 1a) is to use an inverse method, and there are certain advantages to be had by adopting the latter while realizing that often geometric constraints must still be achieved. By adopting an inverse approach, the degree to which the aerodynamic performance can be controlled has reached a high level of sophistication. Inverse design in the classic sense involves specifying a desired velocity distribution (Fig. 1b) based on boundary-layer and consequently performance considerations. Taking this one step further by directly prescribing the desired boundary-layer characteristics (Fig. 1c) is a step closer to controlling the desired outcome—the performance. Thus, employing an inverse boundary-layer-like approach can give the designer tremendous power in achieving the performance goals in the face of all the trade-offs that one must consider in the process of airfoil design. Continuing the sequence in going from geometry based methods to inverse methods, the final step is one wherein the performance is specified using an optimization scheme (Fig. 1d), but implementation of an efficient optimization method has met with limited success relative to the other approaches. Nevertheless, each of these four approaches to design have their respective strengths of allowing more or less direct control over particular characteristics of airfoils. Each of these characteristics could be considered as a design variable (Fig. 1d) that ideally should be incorporated into a single design methodology.

Apart from the design variables of choice, a second consideration involves having the ability to control the performance over multiple operating points. Figure 3 illustrates this concept. Typically, airfoil design requirements include information regarding $C_{l,max}$ (point C in the figure) as well as the operating range over which low drag is achieved (points A

to B). These requirements can be translated into specific characteristics to be embodied in the pressure distribution. For instance, low drag at points A and B requires extended runs of laminar flow on the lower and upper surfaces, respectively, while the high lift requirement is achieved by limiting the leading edge suction peak behavior, each of which must be achieved at the corresponding design lift coefficient. Collectively this approach is referred to as multipoint design, which is clearly a desired feature of any airfoil design method.

3 Laminar Separation Bubbles and Transition

Low Reynolds number airfoil flows are principally distinguished by their associated laminar separation bubbles such as that depicted in Fig. 4. In past research, considerable attention has been focused on laminar separation bubbles because they are the leading culprit to the degradation in performance relative to airfoils at higher Reynolds numbers. When laminar separation bubbles do appear, they are caused by the inabilty of the flow to make a transition to turbulent flow in the attached boundary layer on the surface of the airfoil. Instead, the laminar flow separates before transition. When this happens, transition occurs in the free shear layer, and the so-called laminar separation bubble is formed when the turbulent flow reattaches to the airfoil surface downstream of transition. For the most part, the resulting pressure drag over the region of the laminar separation bubble is responsible for the relatively high drag that can sometimes accompany airfoils at low Reynolds numbers. The existence of a laminar separation bubble and its extents can be deduced by examining surface oil flow visualization as will be discussed later in these notes.

As shown by Drela,[15] the drag contribution owning to a bubble can be approximated by considering the integral boundary layer equation

$$\frac{d\theta}{d\xi} = -(2+H)\frac{\theta}{u_e}\frac{du_e}{d\xi} + 2\,C_f$$

from which the drag coefficient can be determined using

$$C_d = \frac{2(\theta_{us} + \theta_{ls})}{c}$$

For the special purpose here of considering the drag due to a laminar separation bubble, it is more helpful to express the integral boundary layer equation as

$$\frac{1}{\rho u_e^2 \theta}\frac{d(\rho u_e^2 \theta)}{d\xi} = \frac{C_f}{2\,\theta} - \frac{H}{u_e}\frac{du_e}{d\xi}$$

Inside the laminar separation bubble, the skin friction is nearly zero and hence it can be assumed that $C_f \simeq 0$. In this case the integral boundary layer equation becomes

$$\frac{\Delta\rho u_e^2 \theta}{\rho \overline{u}_e^2 \theta} \simeq -H\frac{\Delta u_e}{\overline{u}_e}$$

or

$$\Delta\rho u_e^2 \theta \simeq -\rho \overline{u}_e \delta^* \Delta u_e$$

Thus, the drag increment due to a laminar separation bubble is proportional to the product of the average mass defect $\rho\overline{u}_e\delta^*$ and drop in the edge velocity Δu_e. A graphical interpretation of this result is shown in Fig. 5. Three edge velocity distributions are shown together with the drag increment that grows downstream. For case 1, transition is assumed to have occurred on the airfoil surface without the mechanism of a laminar separation bubble. Prior to transition, the drag increases slowly, while downstream of transition the growth is more rapid and consistent with a turbulent boundary layer. For case 2, laminar separation is shown to have occurred as indicated by the plateau in the velocity distribution, which is accompanied by no growth in the drag increment until transition occurs. At transition and subsequent reattachment, there is a jump in the drag that continues to grow consistent with the turbulent boundary layer behavior. For case 3, a longer laminar separation bubble is considered. In this case, the larger drop in the edge velocity at transition gives rise to a correspondingly larger jump in the drag increment as compared with case 2. Clearly, between the two limiting cases of transition without a bubble (case 1) and transition at the end of a long bubble (case 3), there is an optimum where the bubble drag increment can be minimized. For most airfoils, this minimum case in relation to the total airfoil drag is associated with a thin laminar separation bubble that has only a small drop in the edge velocity at transition.

From this discussion in connection with Fig. 5 that shows the drag increment through a bubble, the location of transition dictates the size of the bubble and with it the drag of the bubble. Thus, an airfoil designer focuses on the questions: where is transition, where should it be, and how can it be controlled? Taken together answers to these questions should yield more knowledge of airfoil flows and help in the development of a design philosophy. As a step in this direction, the following section outlines an approach to finding the transition location, which is the first step in low Reynolds number airfoil design.

4 Finding Transition

As will be seen, having knowledge of the transition location is key to the development of the low Reynolds number airfoil design philosophy presented later. In what follows, two tools for determining transition are discussed—first through experiments and then through predictions.

4.1 Tool #1: Wind Tunnel Tests

All experiments were conducted in the University of Illinois at Urbana–Champaign (UIUC) subsonic wind tunnel (Fig. 6), which has a nominal test section that is 2.81-ft high and 4-ft wide. The test set-up depicted in Figs. 7 and 8 was used for this study.[16,17] As seen in Fig. 7, two 6-ft long Plexiglas splitter plates are inserted 2.8 ft apart into the test section to isolate the airfoil models from both the support hardware and the tunnel side wall boundary layers. The 1-ft chord airfoil models were inserted horizontally between the splitter plates with nominal gaps of 0.040–0.080 in. between the end of the airfoil model and the splitter plates. Performance data were taken at Reynolds numbers of 100,000, 200,000, 350,000 and 500,000. The lift was measured using a strain gauge load cell, and the drag was determined using

the momentum deficit method.[16] To account for spanwise drag variations at low Reynolds numbers,[18] the drag was obtained from an average of eight equidistant wake surveys over the center of the model so that a 10.5-in. wide span was covered. The overall uncertainty in both the lift and drag measurements was estimated at 1.5%.[16,17] All lift and drag measurements were corrected for wind tunnel interference and validated with data from the NASA Langley Low Turbulence Pressure Tunnel.[4,16,18–20]

As has been well documented, low Reynolds number airfoil flows are highly sensitive to the tunnel flow quality. Consequently, tunnel flow quality measurements were taken and documented in detail in Refs. 4 and 21. Only a subset of those results, in particular the turbulence intensity measurements, are included in these lecture notes. The turbulence intensity was measured using hot-wire anemometry. Specifically, the hot-wire system was a TSI Incorporated IFA 100 anemometer in conjunction with a TSI Model 1210-T1.5 hot-wire probe. The probe makes use of a 1.5-micron platinum-coated tungsten wire. The probe was mounted in the tunnel end-flow orientation with the wire perpendicular to the tunnel floor in order to measure the axial turbulence intensity. A PC equipped with a data acquisition card was used to log the signal from the anemometer. A HP 35665A Dynamic Signal Analyzer, which performed a FFT (Fast Fourier Transform) analysis, was employed to allow the turbulence spectrum to be monitored over a broad range of frequencies. More details of the method are given in Ref. 21.

The turbulence intensity was calculated from data using a total of 50,000 samples with a sample frequency of 10,000 Hz. Figure 9 shows the resulting turbulence levels for both the tunnel empty case and with the full measurement apparatus installed. In general these levels are considered to be sufficiently low for taking low Reynolds number airfoil measurements.

The surface oil flow visualization technique made use of a fluorescent pigment (Kent-Moore 28431-1) suspended in a light, household-grade mineral oil that was sprayed onto the surface of the model using a Paasche Model VL double-action airbrush. The model was then subjected to 20–45 min of continuous wind-tunnel run time at a fixed Reynolds number and angle of attack. During this period, the oil moved in the direction of the local flow velocity at a rate dependent on the balance of forces dictated by the boundary-layer skin friction coefficient C_f and surface tension of the oil. As a result, regions of the flow could be identified and compared with the NASA Langley Low-Turbulence Pressure Tunnel (LTPT) data.[19,20]

Figure 10 shows a photograph of the surface oil flow pattern made visible under fluorescent light. Figure 11 conceptually illustrates the connection between the salient surface oil flow features and the skin friction distribution. Note that the skin friction distribution, though conceptual, is consistent with the results of many computational studies.[22–27] The authors believe that the unique shape of the C_f distribution, in particular the strong negative C_f spike, has yet to be experimentally verified (as no experimental data could be found); however, the oil flow patterns observed seem to confirm the validity of the negative C_f spike concept.

Several important flow features can be identified and related to the underlying skin friction and surface tension forces. In Fig. 10, laminar flow is seen to exist from the leading edge to approximately $0.40c$. The oil streaks are characteristically smooth in this region until laminar separation occurs, which is identified in Fig. 11 as the point where $C_f = 0$. (Note again that the flow shown in Fig. 11 is conceptual, and it is not intended to match

Fig. 10 in detail.) Downstream of the point of laminar separation, the original airbrushed "orange-peel" texture that existed prior to running the tunnel still exists, indicating that the flow is stagnant in this region. This stagnant flow is consistent with the known behavior of flow in the interior leading-edge region of a laminar separation bubble. As sketched, the C_f magnitude in this region is quite small due to the low flow speed and negative in sign due to reverse flow at the surface.

In the presence of a laminar separation bubble, transition takes place in the free shear layer above the surface of the airfoil. Downstream of this point, reattachment occurs in a process that is known to be unsteady as vortices are periodically generated and impinge on the airfoil surface.[27,28] These unsteady vortices colliding with the surface lead to a relatively high shear stress that tends to scour away the oil at the mean reattachment point, pushing oil upstream or downstream of the reattachment point. As seen in Fig. 11, the reattachment line is less distinct because the bulk of the oil has been pushed away revealing the underlying black airfoil surface. In Fig. 10, the tunnel run time was long enough that the reattachment line at $0.58c$ is even harder to see than in Fig. 11. In the original high-resolution color photographs that were archived, this feature is clear and easily quantifiable.

Downstream of reattachment the boundary layer is turbulent. The high skin friction in this area relative to the laminar boundary layer upstream tends to clear away more oil, again making the black surface downstream more visible than in the upstream region.

The remaining visible feature of the flow is a line where the oil tends to pool, termed here the "oil accumulation line." This intrinsic feature of the oil flow has no direct connection to laminar flow, reverse flow in the bubble, or the ensuing turbulent flow downstream. However, it does indicate a relatively important feature of the flow with regard to the nature of the skin friction in the vicinity of reattachment. The negative C_f spike shown in predictions and sketched conceptually in Fig. 11 is most likely responsible for generating the oil accumulation line. Assuming that this is the case, the fluctuating high skin friction that is generated over the unsteady reattachment zone will tend to push the oil upstream ahead of the mean reattachment point. At some location on the airfoil, however, the oil moving upstream will experience a balance of forces between the rapidly weakening skin friction force and that of the surface tension and oil adhesion that is retarding its motion. At the location where these two forces balance, the oil accumulates into a line that becomes the most distinguishable feature of the oil flow. Consequently, it is speculated that this flow feature is sometimes mislabeled as "reattachment" as will be discussed below.

4.2 Tool #2: XFOIL Predictions

In the data presented here, XFOIL[14] has been used as a post-design viscous/inviscid analysis tool. A linear-vorticity second-order accurate panel method is used for inviscid analysis in XFOIL. This panel method is coupled with an integral boundary-layer method and an e^n-type transition amplification formulation using a global Newton method to compute the inviscid/viscous coupling, requiring less than a minute of elapse time per polar on modern desktop computers. For the current work n_{crit} was set to the default value of 9, which is typical for a smooth wing surface in a low-turbulence environment. Each airfoil was represented in XFOIL using 230 panels distributed using XFOIL's default paneling routine. XFOIL has proven to be well suited for the analysis of subcritical airfoils even in the presence

of significant laminar separation bubbles.

4.3 Results

XFOIL was used to predict the viscous pressure distributions on the E387 airfoil as shown in Figs. 12a–c. The characteristic pressure distribution caused by the presence of a laminar separation bubble is clearly seen. Oil flow visualization was performed to document the locations of the major surface flow features as presented in Figs. 13, 14, 15, and 16. These results were then compared with benchmark data and also XFOIL predictions.

Figures 17 and 18 show the previously described flow features compared with benchmark data obtained at the NASA Langley LTPT. In the low drag range between -2 deg and 7 deg angle of attack, the agreement in the laminar separation line between the NASA LTPT and UIUC data sets is mostly within $0.01c$ to $0.02c$, which is very near the uncertainty of the method. As previously discussed, the next feature to appear is the oil accumulation line. The UIUC oil accumulation line agrees fairly well with the "reattachment" line identified in the NASA experiment. It is believed, however, that based on the previous reasoning this label given in the original reference[20] is a misnomer. Had the UIUC tests been performed for a longer duration, the reattachment zone would be scoured clean with no remaining distinguishing feature, leaving only the oil accumulation line to be labeled as the "reattachment line," knowing that one must exist. Hence, it is speculated here and in prior UIUC work[17] that such a scenario took place in the NASA study, i.e. the oil-accumulation line was misinterpreted as the reattachment line.

Guided by this working assumption, the two results again are in good agreement. It must be stated, however, that the oil accumulation line might change slightly from one facility to the next since it is dictated by a force balance that depends on the skin friction forces of the boundary layer relative to the adhesion forces of the particular oil used. The predictions, however, show that the negative C_f region has a sharp upstream edge, which is most likely where the oil accumulates regardless of the surface tension characteristics. Differences in the oil accumulation line due to differences in the type of oil used are therefore believed to be small. The good comparisons between UIUC and Langley data tend to support this assumption.

Moving further downstream, the UIUC reattachment data is plotted, but unfortunately no direct comparison can be made because of the ambiguity with respect to the reattachment data reported in the NASA study. However, close inspection of the data suggests that at a Reynolds number of 300,000 and between 5 and 7 deg angle of attack, the LTPT line merges with the UIUC reattachment line. Perhaps in this case, the measurements at Langley were indeed the reattachment points.

The conclusion to be drawn from this comparison of the oil flow visualization results is that the two facilities produce airfoil flows that are in close agreement. Moreover, if the arguments regarding the oil accumulation line are correct, then the agreement can be considered excellent and within the uncertainty of the measurements.

To make comparisons with predictions, the upper-surface flow features for each airfoil were computed at Reynolds numbers of 200,000, 350,000, and 500,000 and at angles of attack from -2 to 18 deg using XFOIL[14] (version 6.94, http://raphael.mit.edu/xfoil/). These data were then used to determine the point of laminar separation and reattachment, which are

both defined by $C_f = 0$ as illustrated in Fig. 11. A comparison between these predictions and experimental measurements are shown in Figs. 19, 20, and 21. The agreement is quite good, and this lends confidence to using XFOIL as an integral tool for analysis of low Reynolds number airfoils.

5 Design Philosophy

As was discussed in Section 3, the performance of low Reynolds number airfoils is strongly dependent on the location of transition as that sets the length of the laminar separation bubble and consequently the magnitude of the drag rise attributable to the bubble. Thus, controlling transition is a key step towards mitigating the adverse effects of laminar separation bubbles on low Reynolds number airfoils.

One common approach to controlling transition, in particular, promoting transition, is to employ an instability region in the pressure gradient or, as it is commonly called, a transition ramp. A general discussion of transition ramps can be found in Refs. 13 and 29, and additional details specific to low Reynolds number airfoils are discussed in Refs. 15, 30, 31, and 32. Figure. 22 shows a concept sketch of a transition ramp on the upper surface velocity distribution. A ramp can be used on either surface of the airfoil, but in these lecture notes attention will be focused on the upper surface. A second approach is to use a turbulator or trip on the airfoil surface, such a zigzag trip like that shown in Fig. 23. Various types of boundary layer trips have been used in the past, but for greatest efficiency three-dimensional trips are believed to be more effective.[33] The remainder of these lecture notes is concerned with the former approach to promoting transition—that of using a transition ramp.

Of critical importance in the design of low Reynolds number airfoils is the upper surface pressure distribution. The tendency of the flow to form a laminar separation bubble can lead to a significant degradation in performance owing to the high bubble drag. To mitigate these adverse effects, a transition ramp in the pressure distribution is often employed to gradually bring the flow to transition in a thin bubble without a large pressure rise and high drag associated with an otherwise thick bubble.

Illustrating a transition ramp by means of showing the pressure distribution (Fig. 22) is instructive, but the essence of a transition ramp can be more precisely defined by examining the movement of transition with angle of attack. Figure 24 shows a concept sketch of a polar and in relation to this the transition locations on both surfaces of the airfoil. As can be seen, over the low drag range, transition on the upper surface is in the vicinity of the midchord of the airfoil. As the angle of attack is increased, transition moves forward as the upper surface pressure gradient becomes more adverse. In these notes, the transition ramp as indicated in Fig. 24 will be defined as the chordwise extent over which transition moves while the airfoil operates in the low drag range of the polar.

Given this approach to defining a transition ramp, consider the Wortmann FX 63-137 airfoil shown in Fig. 25 together with its inviscid pressure distribution. As can be seen, on the upper surface there is a gradual adverse pressure gradient that will promote transition as has been described. Figure 26 shows the measured locations of the major flow features with angle of attack, and in this form the extents of the ramp are more clearly defined. As can be deduced from the figure, transition (which occurs near the point of reattachment)

moves from nearly 80% of chord at low angles of attack to near 20% of chord at an angle of attack of near $\simeq$10 deg. The corresponding performance is shown in Fig. 27. The low drag range of the polar extends from $C_l = 0.5$ to $C_l \simeq 1.6$ which correspond to angles of attack of -2 deg to $\simeq$10 deg, respectively.

In contrast to the FX 63-137 airfoil, which was designed for low Reynolds numbers, the high Reynolds number design NASA NLF(1)-0414F airfoil was also examined. At high Reynolds numbers, the need for a relatively long transition ramp is diminished. Thus, the pressure recovery region can occur rather abruptly so long as transition occurs before recovery. For this reason, a relatively short transition ramp is often employed. On the NASA NLF(1)-0414F airfoil this ramp occurs at $\simeq$70% chord on the upper surface (see Fig. 28). At low Reynolds numbers with a steep pressure recovery occurring this far aft, a long bubble can be expected to occur. Indeed as shown in Fig. 29 laminar separation occurs relatively far aft, and at the lowest Reynolds number of 200,000 reattachment does not occur. For the two higher Reynolds numbers of 350,000 and 500,000, reattachment does occur on the airfoil. However, the resulting long bubble leads to a significant degradation in performance as show in Fig. 30.

The contrast between the FX 63-137 and NASA NLF(1)-0414F airfoils illustrates large performance differences resulting from correspondingly large differences in their respective transition ramps. Even small changes in the shape of the transition ramp, however, can have important effects on performance as follows.

The effect of subtle changes in the transition ramp is demonstrated using two example airfoils A and B. Figure 31 shows a comparison of the geometries and inviscid velocity distributions. These airfoils were designed to each have a different transition ramp that is reflected in a different shape for the transition curve (C_l-x_{tr}/c curve) on the upper surface. The two airfoils were analyzed using XFOIL, and Fig. 32 shows the drag polars and upper-surface transition curves for a Reynolds number of 200,000. As was mentioned, the transition ramp is defined here as the region over which the bubble moves gradually as defined by the transition curve. (In this context, the transition ramp might be more aptly called a "bubble ramp."[31])

From Fig. 32, it can be seen that airfoil A has lower drag than airfoil B at lift coefficients from around 0.3 to around 0.7, above which value airfoil B has lower drag. Also noticeable is the correlation between the drag polar and the shape of the upper-surface transition curve. For the C_l-range from 0.3–0.7, where airfoil A has lower drag, the transition curve for airfoil A is shallower than for airfoil B; that is, there is a larger change in the value of x_{tr}/c for airfoil A than for B. For values of C_l from 0.7–1.2 where airfoil B has lower drag, the transition curve for airfoil B is shallower than for A. This figure shows that the steepness of the transition curve is a direct indication of the bubble drag. By adjusting the shape of this curve, it is therefore possible to tailor the drag polar of an airfoil at low Reynolds numbers.

Figure 32 also includes an overlay of the variation of bubble size ($x_r - x_s$) with C_l. The size of the bubble for each C_l was obtained by determining the chordwise extent over which the skin-friction C_f, as predicted by XFOIL, was less than or equal to zero. Studying the bubble-size variation for the two airfoils further illustrates the connection between the shape of the transition curve and the bubble drag. The bubble is larger when the transition curve is steeper.

Figure 33 shows the inviscid velocity distributions for airfoil A at C_l values of 0.5 and 1.0

with the upper-surface bubble location marked in bold. A similar plot for airfoil B is shown in Fig. 34. Comparing the velocity drops across the bubble for the four cases, it can be seen that while airfoil A has a smaller velocity drop than airfoil B at $C_l = 0.5$, the situation is reversed for $C_l = 1.0$. Since the pressure drag due to the bubble increases with increasing velocity drop across the bubble, airfoil A has smaller bubble drag at the low C_l and larger bubble drag at the higher C_l. Thus, a steeper transition curve results in a larger bubble and also a larger velocity drop across the bubble causing an increase in bubble drag.

The connection between the transition ramp as defined by the C_l-x_{tr}/c transition curve and the resulting performance forms the basis of the present low Reynolds number airfoil design philosophy. The philosophy is to prescribed the C_l-x_{tr}/c transition curve realizing that at most it can extend from the trailing edge to the leading edge. Between these two points (or simply the extent of the ramp) the airfoil performance can be further controlled by prescribing the slope of the curve—the shallower the slope, the lower the drag, and vice versa. There are however tradeoffs that must be addressed as was illustrated in the prior example. The next step involves the implementation of this philosophy into a design methodology.

6 Methodology

In this section, the philosophy of prescribing the C_l-x_{tr}/c transition curve (which in effect is the transition ramp) is conveniently implemented in the inverse design code PROFOIL. First, however, general background on the method and its capabilities are presented, and following this its use in low Reynolds number airfoil design is described.

The PROFOIL code[10,11] embodies an inverse airfoil design method and an integral boundary-layer method for rapid analysis at the design points. The method draws on the pioneering work of Eppler[12,13,34,35] in inverse airfoil design and analysis through conformal mapping (outlined in Figs. 35, 36 and 37) and integral boundary-layer techniques, respectively. PROFOIL differs from the Eppler code in that laminar and turbulent boundary-layer developments can be directly prescribed through iteration on the velocity distribution. The method also allows for control over certain geometric constraints, such as the local geometry, maximum thickness, thickness distribution, etc. Additional differences are discussed in Refs. 10, 11, and 36. Both the boundary-layer and thickness-constraint capabilities are used in the examples presented in these lecture notes. A web-based version of PROFOIL and further discussion is available on the web.[37]

The general capabilities of PROFOIL are illustrated in Figs. 38, 39, and 40. In Fig. 38, three segments of an airfoil (to be designed) are specified to include a velocity distribution, n-development (as used in the e^n method for transition prediction), and H_{12} development, each to be achieved at different conditions. It should be noted that this is merely an example and is not intended to be use for any practical application. Figure 39 shows the solution that includes the relevant characteristics as prescribed, while Fig. 40 shows the final airfoil shape.

For the low Reynolds number airfoil design problem, the design variable of choice is not the geometry nor the velocity, but instead it is the C_l-x_{tr}/c transition curve as illustrated in Figs. 31–34. In coping with this problem of in effect prescribing the C_l-x_{tr}/c transition curve, a useful approach derives from an inherent feature of the Eppler theory for inverse airfoil

design. Briefly, in the Eppler method, the designer can specify for a segment of the airfoil a design angle attack α^* (relative to the zero-lift line) over which the velocity is constant. For instance, the forward upper surface can be defined as one segment and given a design angle of attack of 10 deg ($C_l = 2\pi\alpha_z \simeq 1$). When the resulting airfoil is then operated at 10 deg with respect to the zero-lift angle of attack α_{zl}, the velocity over that segment is then constant. For a higher angle of attack, the resulting pressure gradient is adverse and vice versa. Further discussion can be found in Refs. 13 and 38.

Because (1) the boundary layer responds to the pressure gradient, (2) the design angle of attack α^* for a segment has a direct effect on the pressure gradient, and (3) many such segments can be used to define an airfoil, these three aspects can be connected to yield an elegant solution to having precise control over the C_l-x_{tr}/c transition curve. Figure 41 shows the velocity distributions for the SA7035 airfoil at several design angles of attack. As seen, for segments 8, 9, 10, 11, 12, and 13 the design angles of attack α^* are 1.59, 3.34, 5.07, 6.63, 7.41, and 8.21 deg, respectively. When the airfoil operates at these values of α_z, the velocity gradient over the respective segments is zero as shown in the exploded portion of the figure.

When these design angles of attack α^* are plotted vs. the segment-endpoint arc limits ϕ used in the conformal mapping to generate the airfoil, the resulting curves shown in Fig. 42 mimic the corresponding transition curves over the respective surface of the airfoil, thereby providing a means of controlling the transition ramp and resulting drag as was done also with the example of Figs. 31 and 32. For the SA703x series, the α^*-ϕ curve shown in Fig. 42 maps from leading edge back to segment-endpoint 1 or approximately 75% of the chord (see Fig. 41). It is over this region that the ramp is controlled by the α^*-ϕ curve, with the remainder being controlled by the final trailing edge pressure recovery seen in Fig. 41. The essence of this technique has been employed in the design of most of the S*xxxx four-digit airfoils reported in the literature and archived in Refs. 16, 17, 31, 37, 39, and 40.

The PROFOIL code, which is written in Fortran, has been integrated with a graphical user interface (GUI) using Matlab. This GUI code, given the name MFOIL, allows the user to interactively modify the α^*-ϕ curve and view the resulting changes in the airfoil and corresponding velocity distributions. Sample screen grabs of the code are show in Figs. 43 and Fig. 44.

The remainder of these notes are devoted to applications of the methodology.

7 SD7003 and SD2030 Airfoil for F3B Model Sailplanes

This first example airfoil, the SD7003, was designed in 1989 and documented in Ref. 31. Originally it was intended for F3B R/C soaring competition, and at the time of its design its overall drag characteristics were predicted and measured to be the lowest of several competing sections. Figure 45 shows the airfoil and inviscid velocity distributions while Fig. 46 shows the α^*-ϕ curve.

What distinguishes this airfoil from many others is the rather long and quite shallow transition ramp as seen in Figs. 47, 48, and 49 and as is consistent with the shape of the α^*-ϕ curve. In fact, the upper surface transition ramp extends along the entire length of the airfoil. The shallow ramp yields a thin bubble and consequently little associated bubble drag as can be deduced from the polars shown in Fig. 50. Several attempts were made to

reduce the drag through the use of turbulators, but they either increased the drag or had no effect as documented in Ref. 31. This fact is further evidence that the bubble drag is quite small for this section. Another interesting observation is that as compared with the E387 (and several other airfoils) the oil flow on the surface of the SD7003 was more smeared without the high degree of flow feature definition seen in Fig. 10.

During this exploratory period in 1989 when there was generally less known about low Reynolds number airfoils, a second F3B airfoil, the SD2030 shown in Fig. 51, was designed for higher Reynolds number operation with the use of camber changing flaps. The design philosophy was opposite that of the SD7003 in that the bubble ramp was rather short and positioned far aft on the airfoil. Although the α^*-ϕ curve is not shown, it mirrors the shape of the C_l-x_{tr}/c transition curve that is shown together with the polar in Fig. 52. As compared with the SD7003, the ramp on the SD2030 is steeper and occurs further aft on the airfoil. From this information alone, one would expect the drag to be higher at the lower Reynolds numbers, and this is indeed the case as seen in the predictions (Fig. 52) and measured performance shown Fig. 53. For Re = 500,000, however, the extended runs of laminar flow give rise to lower drag than the SD7003, which was one of the original design goals. (It is worth noting the generally good agreement between the XFOIL predictions and experiment, particularly at a Reynolds number of 200,000. The model in this case was accurate to 0.006 inch for the 12-inch chord model that was tested.[4] In comparison, the SD7003 was accurate to 0.004 inch.[31])

8 SG604x Series for Small Wind Turbines

The SG604x series of airfoils[41] as shown in Fig. 55 was designed for small variable-speed horizontal-axis wind turbines having a rated-power of 1–5 kW. The operational Reynolds number for such machines is typically below 1,000,000. The focus here will be on the performance at a Reynolds number of 300,000, which represents rotors on the lower end of the range. In ideal conditions, variable speed wind turbines operate at a constant tip speed ratio ($\Omega R/V_\infty$), which leads to the airfoil operating at a single angle of attack over a wide range of wind speeds. As a result, for optimum aerodynamic performance during variable-speed operation, the low-drag lift range (drag bucket) can be reduced in favor of having greater lift-to-drag ratios. However, to account for possible variations in the tip-speed-ratio caused by atmospheric turbulence and operational considerations, the best lift-to-drag ratio conditions should occur over a range of lift coefficients centered about the design lift coefficient. In rotor design, another factor deals with the trade-off between the blade solidity and the design lift coefficient. With all else being equal, a high-solidity rotor requires an airfoil with lower lift than that required for a low-solidity rotor. Therefore, given the range of rotor designs, a family of airfoils that cover a range of lift coefficients is desirable. These general considerations and others were taken into account in setting the design requirements as detailed more thoroughly in Ref. 41. The current discussion is mainly concerned with the details of the design approach.

PROFOIL was used to prescribe the desired aerodynamic characteristics. In a manner similar to that used in the previously discussed SD7003 and SD2030 airfoils, the α^*-ϕ curve was prescribed to define the desired shape of the C_l-x_{tr}/c transition curve. Since the objective

was to achieve a high lift-to-drag ratio with less emphasis being given to operation over a wide range, the ramp on the upper surface was made to be rather shallow at the specific design lift coefficients of 0.6, 0.9 and 1.2 for the SG6041, SG6042, and SG6043, respectively. Additional constraints included the pitching moment, which increased with the design lift coefficient and also the airfoil thickness of 10%. It should be added that for ease of construction a finite trailing-edge angle was used, producing a zero trailing-edge velocity as seen in Fig. 55.

Performance predictions at a Reynolds number of 300,000 are shown in Fig. 56 and compare relatively well with the experimental results of Fig. 57. Most importantly, the trends in the predictions agree well with experiment, and also the behavior of the α^*-ϕ curve is reflected in the transition curve (Fig. 56).

Figure 58 shows the resulting experimentally-determined lift-to-drag ratios at a Reynolds number of 300,000 as compared with those for many previously existing airfoils. The SG6040 shown in the figure is the thicker companion root airfoil for the series of tip airfoils discussed here. Clearly, the objective of achieving high lift-to-drag ratios has been achieved. Given the high level of performance, these airfoils will likely find their way into applications beyond wind energy.

9 S607x Series Designed for Low Pitching Moment

The S607x series is composed of three series of three airfoils each. The effort finally lead to an airfoil for its intended application that required a low pitching moment and optimum performance at a Reynolds number of 150,000 and lift coefficient near 1. Only data for a Reynolds number of 200,000 is presented here, however. The series evolved from a 9%-thick family to 12%, and then permutations in the pitching moment were made while other improvements were incorporated. In these lecture notes only the second two series are discussed.

For the second series (S6074/5/6), the study centered on the upper-surface transition ramp. Figure 59 shows the small changes in the α^*-ϕ curve to optimize the transition ramp so as to achieve optimum performance near $C_l \simeq 1$. These differences result in small changes to the resulting velocity distributions shown in Fig. 60. As seen, the shallower α^*-ϕ curve for airfoil S6076 results in a shallower pressure gradient over the forward upper surface. The differences in the airfoil shapes are so minute that a magnification of the y-axis is needed to highlight the differences. These small changes to the ramp, however, do have a significant effect on the bubble as may be deduced from the wind-tunnel tests results depicted in Fig. 61.

Unfortunately, this series exhibited undesirable hysteresis as seen in the lift and moment curves shown in Fig. 62. The occurance of hysteresis sometimes found at low Reynolds numbers (as in this case) cannot be predicted by any computational method. However, should hysteresis arise, an attempt can be made to reduce the amount of hysteresis or eliminate it entirely. The first steps toward this remedy requires some understanding of the flow phenomenon.

Figure 63 shows two types of hysteresis that sometimes appear on low Reynolds number airfoils. The flow states corresponding to points A and B on opposite branches of the hysteresis loops is sketched in Fig. 64. For case A, a short laminar separation bubble exists on the upper surface near the leading edge. Downstream of this point the flow is mostly

attached, but some trailing edge separation (not sketched) may exist. For case B, the flow is in a stalled state, and laminar flow extends to the point of separation, which occurs near the midchord or even closer to the leading edge. As shown both of these flow states are possible at the same angle of attack (as indicated in Fig.63), and hence there is hysteresis.

What separates and distinguishes the two cases shown in Fig. 63 is the order in which flow states A and B occur. For the clockwise hysteresis loop, when the angle of attack is decreasing out of stall on the lower branch, the flow is first massively separated. Then at a certain point, a small bubble is formed and the lift jumps to the upper branch. For the counter clockwise loop, the opposite situation occurs. First, a small bubble resides near the leading edge, and then it bursts and jumps to the lower branch where there is massive separation. When the angle of attack is increased from the normally attached flow condition, the description follows along similar lines except the flow states are reversed.

For the current series, the clockwise hysteresis loop is present. Its elimination depends on a short bubble attaching to the leading edge as the airfoil comes out of stall with decreasing angle of attack. To promote the formation of this bubble, one strategy involves making the leading edge suction peak stronger, thereby causing a leading edge bubble and hence transition to form sooner. This approach was taken.

Figure 65 shows the resulting S6077/9 designs (S6078 is omitted) that have stronger suction peaks as compared with the prior series. A secondary purpose of this final series was to examine the effects of a change in the pitching moment, which was specified using the inverse capabilities of PROFOIL. In comparing the velocity distributions shown in Fig. 60 with those in Fig. 65, it is seen that this current series has a more concave velocity distribution on the forward upper surface to further promote the early formation of a leading edge laminar separation bubble. This difference is reflected in the shapes of the S6074/6 vs. S6077/9. As seen in Fig. 67, this change in the velocity distribution is enough to practically eliminate the stall hysteresis. Finally, the performance is shown in Fig. 68. One feature of using a more concave distribution is that the α^*-ϕ curve (not shown) becomes more shallow. As a result, the laminar separation bubble drag is reduced at the upper corner of the low drag range, yielding lower drag than the S6074/6 airfoils but also lower maximum lift as a tradeoff.

10 S1223 High Lift Section

Increased payloads, shortened takeoff and landing distances, reduced aircraft noise, and lowered stall speeds can all be derived from the beneficial effects of improved high-lift airfoil aerodynamics. It is, therefore, not surprising that the classic problem of high-lift airfoil design has been and remains a topic of considerable interest.[13,42–44] The purpose here is to present a high-lift airfoil design philosophy for the increasingly important low Reynolds number regime in which small unmanned aerial vehicles (UAVs) operate. Only single-element airfoils are considered here.

Airfoils for such aircraft typically operate in the Reynolds number range 200,000 to 500,000. For example, U.S. Navy electronic warfare UAVs (e.g., LAURA[45] and FLYRT[46,47] aircraft) fly at ship-like speeds ranging from 25 to 40 knots with payload requirements varying from 10 to 25 lbs. The small vehicle size required for efficient shipboard storage coupled with low flight speeds and demanding payload requirements places great emphasis

on high-lift low Reynolds number aerodynamics. A similar-sized aircraft, the hand-launched Pointer UAV operated by the U.S. Army,[48] is used to perform short-range reconnaissance missions. Moreover, small payload-laden UAVs have been envisioned for missions that involve atmospheric sampling, border surveillance, forest fire detection/tracking, ship- or aircraft-wreck survivor search and weather monitoring. In each case, high-lift airfoil performance can to varying degrees play an important role.

To place the current work in a proper global context, Fig. 69 presents the maximum lift characteristics of a number of representative low-speed airfoils taken from various sources documented in Ref. 1. Although not all of these airfoils were specifically designed for high-lift, a predictable and anticipated trend emerges—the lower the Reynolds number, the lower the maximum lift. In particular, in going from a Reynolds number of 1×10^6 to 1×10^5, a sharp drop in $C_{l,max}$ is seen in the available data. The lower end of this range is of interest in the design of small UAVs based on current trends.[46] In particular, this section of the notes focuses on high-lift airfoil design for a Reynolds number of 200,000.

It should be mentioned that high lift is rarely the only desirable feature of an airfoil. The airfoil lift-to-drag ratio, endurance parameter, thickness, pitching moment, stall characteristics and sensitivity to roughness are all important factors, among others, that must each be weighed separately when one considers selecting or designing an airfoil. This study focuses on those factors most related to enhanced high-lift low Reynolds numbers airfoil performance.

Based on an analysis of several high lift sections, Fig. 70 shows the pitching moment characteristics vs. the type of upper-surface pressure recovery for several airfoils. The FX 63-137 with its relatively high (negative) pitching moment and convex pressure recovery appears towards the upper left corner. In contrast, airfoils with a Stratford-like concave pressure recoveries and low pitching moments, such as the Miley M06-13-128 airfoil,[43] appear on the lower right. Also shown in the Fig. 70 are several trend lines that, together with the moment and recovery-type information, can be used to deduce a strategy for high-lift low Reynolds number airfoil design. It should be noted that the figure is used to only illustrate the trends and qualitative ideas discussed. Thus, it is not intended to be wholly accurate with respect to the placement of the airfoils. For instance, two airfoils can have the same pitching moment and similar recovery distributions and hence occupy the same point on the plot, yet these two airfoils could exhibit different camber, $C_{l,max}$ and stall characteristics. In the figure, the airfoils are placed most accurately with respect to the $C_{l,max}$ and shape of the recovery distribution.

One trend depicted in Fig. 70 is that an airfoil typically becomes more cambered when the pitching moment increases and/or when the recovery becomes less concave and more convex. Another trend is that the trailing-edge stall becomes more abrupt as the pressure recovery becomes less convex and more concave. "Stall rate" (as denoted in Fig. 70) refers to the shape of the lift curve at stall. The FX 63-137 is an example of an airfoil with a "slow" trailing-edge stall for which the point of turbulent separation slowly progresses forward as the angle of attack increases. The M06-13-128 is an example of an airfoil that has a "moderate" trailing-edge stall.[1] The lift curve peaks at $C_{l,max}$, then falls off more rapidly than the FX 63-137 airfoil. This characteristic is indicative of a turbulent separation point that moves forward more quickly with increasing angle of attack.

The last trend shown in Fig. 70 is that the maximum lift coefficient increases as the

pitching moment increases and as the pressure recovery approaches that of a Stratford distribution. The FX 63-137 is a good example of increasing the $C_{l,max}$ primarily through added pitching moment. In contrast, classic Liebeck-type airfoils[49] (such as the M06-13-128) are good examples of increasing the $C_{l,max}$ mainly through the use of a Stratford distribution.

Specifically, the Liebeck high-lift design philosophy[10] involves using a Stratford distribution to recover the most pressure without separation at $C_{l,max}$. Since separation is avoided entirely, the prototypical Liebeck airfoil is one with no aft loading, which yields a low pitching moment. The M06-13-128 serves as an example of applying the Liebeck design philosophy at low Reynolds numbers. Although the M06-13-128 has a high mid-range bubble drag at the off-design Reynolds numbers of 300,000, the $C_{l,max}$ is approximately 1.5. This value for $C_{l,max}$ is high, especially in light of the intrinsic low pitching moment.

It is discussed by Eppler[13] that to achieve maximum lift on an airfoil with a concave Stratford-like recovery the low pitching-moment constraint should be relaxed. In a computational study for Reynolds numbers above 1×10^6, Eppler showed that the lift of an airfoil with a concave recovery can be increased through the use of aft loading. The airfoils incorporated the favorable effects of both a concave recovery distribution and added pitching moment to achieve high $C_{l,max}$ values. In Fig. 70, airfoils of this type would appear between the FX 63-137 and M06-13-128, but displaced in the direction of increased lift.

As further discussed in Ref. 1, these considerations and others were used to design an airfoil with $C_{l,max}$ greater than 2 for a Reynolds number of 200,000. Figure 71 shows the inviscid velocity distributions predicted by the Eppler code[12] for the S1223 for $C_l = 1.95$. Through the use of PROFOIL, the upper-surface velocity distribution corresponding to the design $C_{l,max}$ was determined from a specified boundary-layer development. In particular, from the leading edge to near $0.20c$, the boundary layer was prescribed to be near laminar separation, an approach that could be considered as a "laminar analogy" to the turbulent Stratford pressure recovery.[50,51] At $0.20c$, a short bubble ramp was employed. The main pressure recovery was prescribed by specifying the turbulent boundary layer to be increasingly near turbulent separation toward the trailing edge. Finally, aft loading was employed at the trailing edge since, as discussed, the penalty due to limited trailing-edge separation is expected to be more than offset by the gain in $C_{l,max}$.

Measured lift characteristics for a Reynolds number of 200,000 are shown in Fig. 72. The results indicate a $C_{l,max}$ of approximately 2.2, which clearly validates the aforementioned design philosophy. As compared with the $C_{l,max}$ of 1.75 for the FX 63-137, a $C_{l,max}$ of 2.2 for the S1223 represents a 25% increase. It should be noted that the S1223 exhibits acceptable moderate stall characteristics much like the M06-13-128. This characteristic is important for some UAVs that operate with the airfoil near $C_{l,max}$ to achieve low-speed flight requirements for loiter, cruise or landing.

In an effort to increase the $C_{l,max}$ of the S1223, it was tested with vortex generators (VGs) located on the upper surface at $0.17c$ and, separately, with a $0.01c$ Gurney flap.[1] The VGs produced a $C_{l,max}$ of 2.3 for increasing angles of attack followed by an abrupt stall and a hysteresis loop. Thus, the VGs as tested were not beneficial. The lift performance with the Gurney flap yielded a $C_{l,max}$ of 2.3, and the stall was much like that of the clean airfoil.

Drag data was taken on the S1223 and is shown in Fig. 73. When the drag coefficient exceeded approximately 0.05, no further data was taken since the airfoil was partially stalled in which case the accuracy of the wake rake measurements are suspect. As compared with the

FX 63-137, the S1223 has higher drag, which is an expected tradeoff for such high maximum lift coefficients.

11 SA703x Series for Thermal Duration Sailplanes

This last example presents a series of airfoils for application to radio controlled (R/C) model aircraft, specifically R/C soaring. The interest in designing such a series was motivated by the results of a survey at the 1996 AMA Nationals/Unlimited Thermal Soaring Category that showed of the 101 responses (from nearly all of the participants) 40 of the pilots used the SD7037 airfoil[31] shown in Fig. 74 together with its inviscid velocity distribution. Two other airfoils (S3021 and RG15) each numbered 8 in use, followed by the fourth (SD7080) with 6, and then 24 different airfoils were used on the remainder. Despite the overwhelming popularity of the SD7037, it was obvious that this airfoil could not be the optimum for a wide range of sailplanes with different sizes, wing loadings and weather conditions. For example, in some situations pilots would benefit by having a faster version of the SD7037 (lower lift), and in others a slower version (higher lift) might be preferable. Thus, the SD7037 became the baseline for this series.

For the series, the objective was to produce a range of similar performing airfoils that differed with respect to their lift range. One approach would be to make simple camber changes to the SD7037 to arrive at the new airfoils, but this process was not used because it is more attractive to control the performance by using the inverse capabilities in PROFOIL. In particular, PROFOIL was used to set the lower corner of the polar by specifying that the laminar boundary layer on the lower surface be close to separating at the lift coefficient at the lower corner of the polar. The shape of the polar above this lift coefficient was then obtained by tailoring the upper surface transition ramp as was discussed (see Fig. 42).

Figure 75 shows the particular laminar boundary-layer development prescribed for the lower corner of the polar. This boundary-layer shape parameter H_{12} distribution, which is close to laminar separation, was specified to be achieved at the design angles of attack of 1.75, 2.15, 2.55 and 2.95 deg relative to the zero-lift line to produce each respective airfoil of the SA703x series shown in Fig. 76. (The SA7037 mimics the baseline SD7037.) In the figure, the velocity distributions are plotted at angle of attack increments equal to those that separate the aforementioned lower surface design angles of attack. The corresponding boundary-layer shape parameter developments as predicted by XFOIL for the lower surface design condition are shown in Fig. 77, and they are practically identical to the prescription shown in Fig. 75. It is worth noting that the laminar boundary-layer H_{12} developments are plotted for a Reynolds number of 200,000; however, the laminar development to transition is independent of the Reynolds number as discussed in Ref. 13.

When each airfoil is operated below the respective design angle of attack for the lower surface, laminar separation and subsequent transition in the laminar separation bubble quickly move forward and lead to higher drag at the end of the low drag range. This result is found in the predictions of XFOIL shown in Fig. 78 and validated by the wind tunnel test results shown in Fig. 79. (In place of the SA7037, the baseline SD7037 was tested.) Additional data for these airfoils over the Reynolds number range from 100,000 to 300,000 can be found in Ref. 17, and tabulated data is available from the web.[37]

12 Conclusions

In these lecture notes, an approach to the design of low Reynolds number airfoils was described. The power of modern computational tools for low Reynolds number airfoil design and analysis was discussed with several examples illustrating the overall approach. Emphasis was placed on the design of the airfoils based on boundary-layer considerations related to the laminar separation bubble and transition. More specifically, the parameterization of the design problem centered around prescribing desirable boundary-layer features through an inverse method. Formulating the design problem in this way offers the designer considerably more power than one would otherwise have using more traditional methods of inverse design (based on a single-point velocity distribution) and design by geometric perturbation. The design approach and philosophy can be used successfully to assess design trade-offs with a high degree of control. Finally, wind-tunnel testing of low Reynolds number airfoils is, however, still needed to provide engineers with a necessary level of confidence required to make important engineering decisions.

References

[1] Guglielmo, J. J. and Selig, M. S., "High-Lift Low Reynolds Number Airfoil Design," *Journal of Aircraft*, Vol. 34, No. 1, January–February 1997, pp. 72–79.

[2] Selig, M. S., Gopalaratham, A., Giguére, P., and Lyon, C. A., "Systematic Airfoil Design Studies at Low Reynolds Numbers," *Fixed and Flapping Wing Aerodynamics for Micro Air Vehicle Applications*, edited by T. J. Mueller, Vol. 195 of *Progress in Astronautics and Aeronautics Series*, AIAA, New York, 2001, pp. 143–167.

[3] McGranahan, B. H. and Selig, M. S., "Surface Oil Flow Measurements on Several Airfoils at Low Reynolds Numbers," AIAA Paper 2003–4067, June 2003.

[4] Selig, M. S. and McGranahan, B. D., "Wind Tunnel Aerodynamic Tests of Six Airfoils for Use on Small Wind Turbines," AIAA Paper 2004–1188, January 2004.

[5] Mueller, T. J., "Low Reynolds Number Vehicles," AGARDograph 288, February 1985.

[6] Mueller, T. J., editor, *Proceedings of the Conference on Low Reynolds Number Airfoil Aerodynamics*, UNDAS-CP-77B123. University of Notre Dame, Notre Dame, IN, June 1985.

[7] *Aerodynamics at Low Reynolds Numbers* $10^4 < Re < 10^6$ *International Conference*, The Royal Aeronautical Society, sponsored by U.S. Office of Naval Research. London Branch, October 1986.

[8] Mueller, T. J., editor, *Low Reynolds Number Aerodynamics*, Vol. 54 of *Lecture Notes in Engineering*. Springer-Verlag, New York, June 1989.

[9] Mueller, T. J., editor, *Fixed and Flapping Wing Aerodynamics for Micro Air Vehicle Applications*, Vol. 195 of *Progress in Astronautics and Aeronautics Series*. AIAA, New York, 2001.

[10] Selig, M. S. and Maughmer, M. D., "A Multi-Point Inverse Airfoil Design Method Based on Conformal Mapping," *AIAA Journal*, Vol. 30, No. 5, May 1992, pp. 1162–1170.

[11] Selig, M. S. and Maughmer, M. D., "Generalized Multipoint Inverse Airfoil Design," *AIAA Journal*, Vol. 30, No. 11, November 1992, pp. 2618–2625.

[12] Eppler, R. and Somers, D. M., "A Computer Program for the Design and Analysis of Low-Speed Airfoils," NASA TM 80210, August 1980.

[13] Eppler, R., *Airfoil Design and Data*, Springer-Verlag, New York, 1990.

[14] Drela, M., "XFOIL: An Analysis and Design System for Low Reynolds Number Airfoils," *Low Reynolds Number Aerodynamics*, edited by T. J. Mueller, Vol. 54 of *Lecture Notes in Engineering*, Springer-Verlag, New York, June 1989, pp. 1–12.

[15] Drela, M., "Low Reynolds-Number Airfoil Design for the M.I.T. Daedalus Prototype: A Case Study," *AIAA Journal*, Vol. 25, No. 8, August 1988, pp. 724–732.

[16] Selig, M. S., Guglielmo, J. J., Broeren, A. P., and Giguère, P., *Summary of Low-Speed Airfoil Data, Vol. 1*, SoarTech Publications, Virginia Beach, Virginia, 1995.

[17] Lyon, C. A., Broeren, A. P., Giguère, P., Gopalarathnam, A., and Selig, M. S., *Summary of Low-Speed Airfoil Data, Vol. 3*, SoarTech Publications, Virginia Beach, Virginia, 1998.

[18] Guglielmo, J. J. and Selig, M. S., "Spanwise Variations in Profile Drag for Airfoils at Low Reynolds Numbers," *Journal of Aircraft*, Vol. 33, No. 4, July–August 1996, pp. 699–707.

[19] Evangelista, R., McGhee, R. J., and Walker, B. S., "Correlation of Theory to Wind-Tunnel Data at Reynolds Numbers below 500,000," *Low Reynolds Number Aerodynamics*, edited by T. J. Mueller, Vol. 54 of *Lecture Notes in Engineering*, Springer-Verlag, New York, June 1989, pp. 131–145.

[20] McGhee, R. J., Walker, B. S., and Millard, B. F., "Experimental Results for the Eppler 387 Airfoil at Low Reynolds Numbers in the Langley Low-Turbulence Pressure Tunnel," NASA TM 4062, October 1988.

[21] Selig, M. S. and McGranahan, B. D., "Wind Tunnel Aerodynamic Tests on Six Airfoils for Use on Small Wind Turbines," NREL report in preparation, 2004.

[22] Briley, R. W. and McDonald, H., "Numerical Prediction of Incompressible Separation Bubbles," *Journal of Fluid Mechanics*, Vol. 69, No. 4, 1975, pp. 631–656.

[23] Kwon, O. K. and Pletcher, R. H., "Prediction of Incompressible Separated Boundary Layers Including Viscous-Inviscid Interaction," *Transactions of the ASME*, Vol. 101, December 1979, pp. 466–472.

[24] Davis, R. L. and Carter, J. E., "Analysis of Airfoil Transitional Separation Bubbles," NASA CR-3791, July 1984.

[25] Walker, G. J., Subroto, P. H., and Platzer, M. F., "Transition Modeling Effects on Viscous/Inviscid Interaction Analysis of Low Reynolds Number Airfoil Flows Involving Laminar Separation Bubbles," ASME Paper 88-GT-32, 1988.

[26] Huebsch, W. W. and Rothmayer, A. P., "The Effects of Small-Scale Surface Roughness on Laminar Airfoil-Scale Trailing Edge Separation Bubbles," AIAA Paper 98-0103, January 1998.

[27] Alam, M. and Sandham, N. D., "Direct Numerical Simulation of 'Short' Laminar Separation Bubbles with Turbulent Reattachment," *Journal of Fluid Mechanics*, Vol. 403, 2000, pp. 223–250.

[28] Lin, J. C. M. and Pauley, L. L., "Low-Reynolds-Number Separation on an Airfoil," *AIAA Journal*, Vol. 34, No. 8, 1996, pp. 1570–1577.

[29] Wortmann, F. X., "Progress in the Design of Low Drag Airfoils," *Boundary Layer and Flow Control*, edited by G. V. Lachmann, London, 1961, pp. 748–770.

[30] Selig, M. S., "The Design of Airfoils at Low Reynolds Numbers," AIAA Paper 85-0074, January 1985.

[31] Selig, M. S., Donovan, J. F., and Fraser, D. B., *Airfoils at Low Speeds*, Soartech 8, SoarTech Publications, Virginia Beach, Virginia, 1989.

[32] Donovan, J. F. and Selig, M. S., "Low Reynolds Number Airfoil Design and Wind Tunnel Testing at Princeton University," *Low Reynolds Number Aerodynamics*, edited by T. J. Mueller, Vol. 54 of *Lecture Notes in Engineering*, Springer-Verlag, New York, June 1989, pp. 39–57.

[33] Hama, F. R., "An Efficient Tripping Devices," *Journal of the Aeronautical Sciences*, Vol. 24, March 1957, pp. 236–237.

[34] Eppler, R., "Direkte Berechnung von Tragflügelprofilen aus der Druckverteilung," *Ingenieur-Archive*, Vol. 25, No. 1, 1957, pp. 32–37, (translated as "Direct Calculation of Airfoil from Pressure Distribution," NASA TT F-15, 417, 1974).

[35] Eppler, R., "Ergebnisse gemeinsamer Anwendung vo Grenzschicht- und Potentialtheorie," *Zeitschrift für Flugwissenschaften*, Vol. 8, No. 9, 1960, pp. 247–260, (translated as "Results of the Combined Application of Boundary Layer and Profile Theory," NASA TT F-15, 416, March 1974).

[36] Selig, M. S., *Multi-Point Inverse Design of Isolated Airfoils and Airfoils in Cascade in Incompressible Flow*, Ph.D. thesis, The Pennsylvania State University, College Park, Pennsylvania, May 1992.

[37] Selig, M. S., *UIUC Applied Aerodynamics Group, PROFOIL—Airfoil Design System, http://www.profoil.org*, University of Illinois at Urbana–Champaign.

[38] Gopalarathnam, A. and Selig, M. S., "Low Speed NLF Airfoils: A Case Study in Inverse Airfoil Design," AIAA Paper 99-0399, January 1999.

[39] Selig, M. S., Lyon, C. A., Giguère, P., Ninham, C. N., and Guglielmo, J. J., *Summary of Low-Speed Airfoil Data, Vol. 2*, SoarTech Publications, Virginia Beach, Virginia, 1996.

[40] Selig, M. S., *The Design of Airfoils at Low Reynolds Numbers*, Soartech 3, SoarTech Publications, Virginia Beach, Virginia, July 1984.

[41] Giguère, P. and Selig, M. S., "New Airfoils for Small Horizontal Axis Wind Turbines," *ASME Journal of Solar Energy Engineering*, Vol. 120, May 1998, pp. 108–114.

[42] Liebeck, R. H. and I., A., "Optimization of Airfoils for Maximum Lift," *Journal of Aircraft*, Vol. 7, No. 5, May 1970, pp. 409–415.

[43] Miley, S. J., "On the Design of Airfoils for Low Reynolds Numbers," *AIAA/MIT/SSA 2nd International Symposium of the Technology and Science of Low-Speed and Motorless Flight*, Soaring Society of America, Los Angeles, CA, 1974, pp. 82–96, also AIAA Paper 74-1017, Sept 1974.

[44] Wortmann, F. X., "The Quest for High Lift," *AIAA/MIT/SSA 2nd International Symposium of the Technology and Science of Low-Speed and Motorless Flight*, Soaring Society of America, Los Angeles, CA, 1974, pp. 97–101, also AIAA Paper 74-1018, Sept 1974.

[45] Foch, J. R. and Toot, P. L., "Flight Testing Navy Low Reynolds Number (LRN) Unmanned Aircraft," *Low Reynolds Number Aerodynamics*, edited by T. J. Mueller, Vol. 54 of *Lecture Notes in Engineering*, Springer-Verlag, New York, June 1989, pp. 407–417.

[46] Foch, R. J. and Ailinger, K. G., "Low Reynolds Number, Long Endurance Aircraft Design," AIAA Paper 92–1263, February 1992.

[47] Bovais, C. and Toot, P. L., "Flight Testing the Flying Radar Target (FLYRT)," AIAA Paper 94–2144, June 1994.

[48] Karch, L. G., "Very Low Cost UAVs: Why We Need Them, What More We Need to Do," *Marine Corps Gazette*, March 1991, pp. 54–57.

[49] Liebeck, R. H., "Design of Subsonic Airfoils for High Lift," *Journal of Aircraft*, Vol. 15, No. 9, 1978, pp. 547–561.

[50] Drela, M. and Giles, M. B., "Viscous-Inviscid Analysis of Transonic and Low Reynolds Number Airfoils," *AIAA Journal*, Vol. 25, No. 10, October 1987, pp. 1347–1355.

[51] Somers, D. M., "Subsonic Natural-Laminar-Flow Airfoils," *Natural Laminar Flow and Laminar Flow Control*, edited by R. W. Barnwell and M. Y. Hussaini, Springer-Verlag, New York, 1992, pp. 143–176.

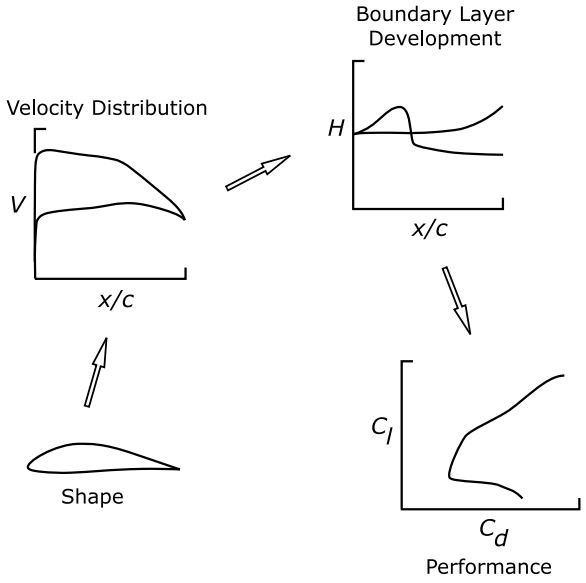

(a) Direct design methods

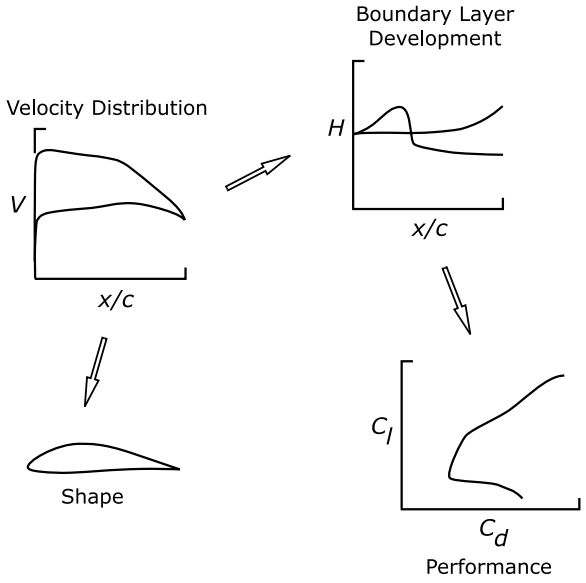

(b) Inverse method via velocity distributions

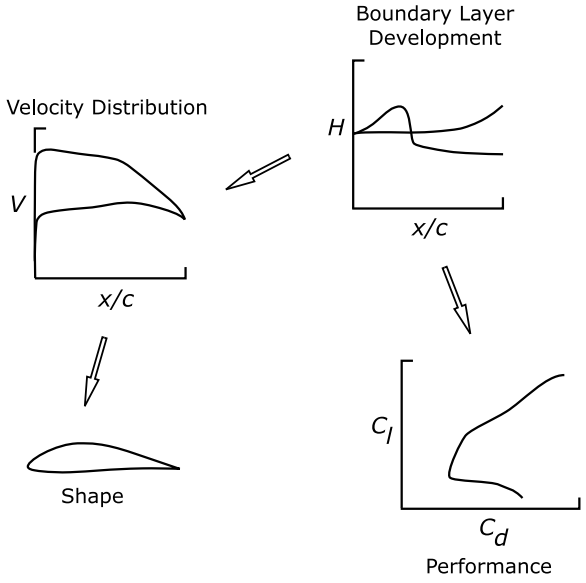

(c) Inverse viscous design (H_{12} shown in conceptual example)

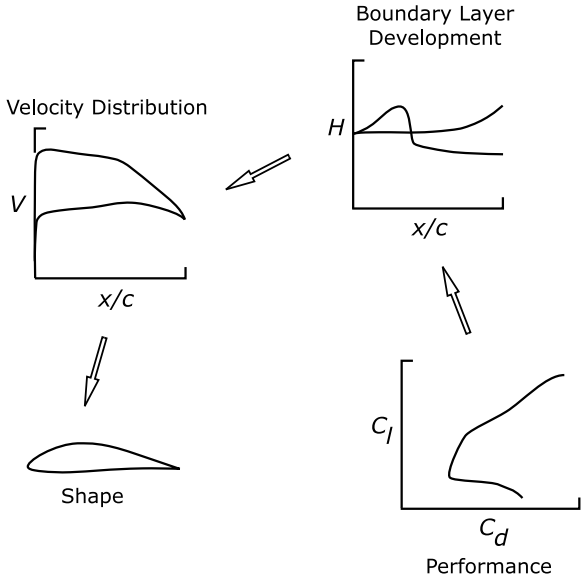

(d) Optimization methods that optimize performance

Figure 1: Various approaches to airfoil design.

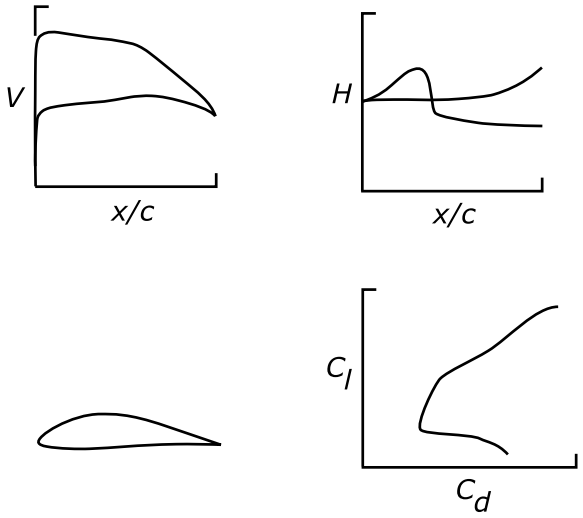

Figure 2: Design variables that should be considered: velocity distribution, boundary layer developments, airfoil geometry, and performance.

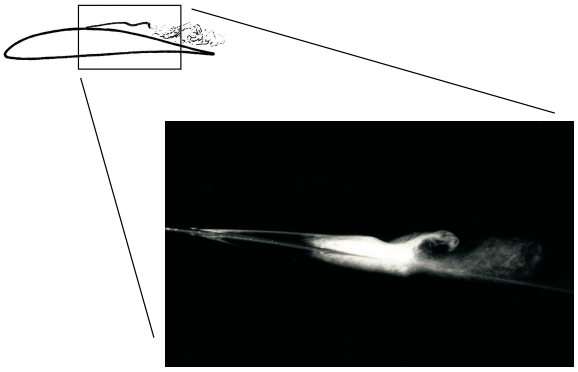

Figure 4: Smoke flow visualization of a laminar separation bubble on the E387 airfoil at a $\boldsymbol{Re} = 100{,}000$, $\alpha = 2$ deg. (*Photo courtesy of Prof. T.J. Mueller and G. M.Cole, University of Notre Dame, 1990.*)

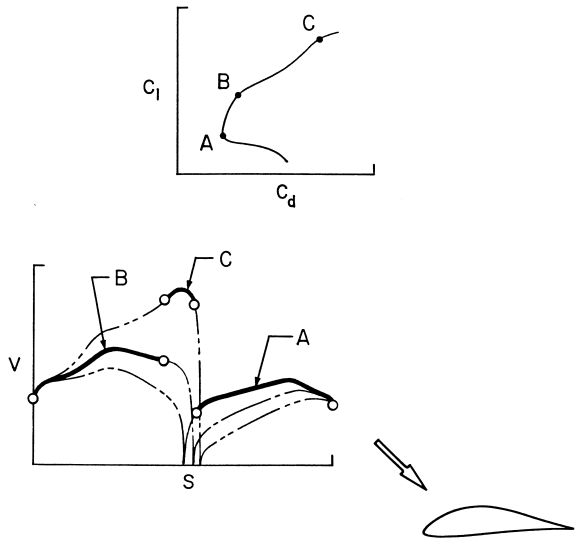

Figure 3: Multipoint design considerations in connection with the desired airfoil performance and corresponding velocity distribution that gives rise to that performance.

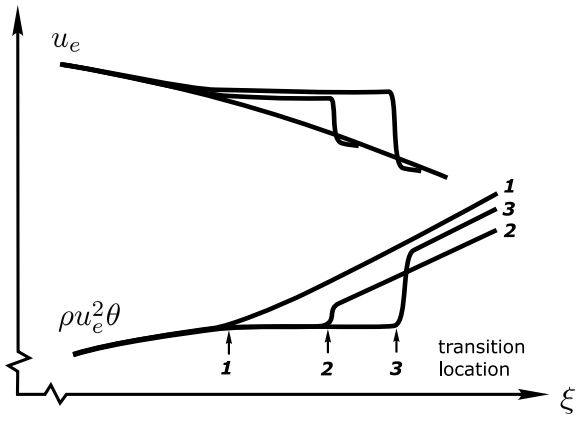

Figure 5: Effect of transition location on bubble size and drag increment (adapted from Drela[15]).

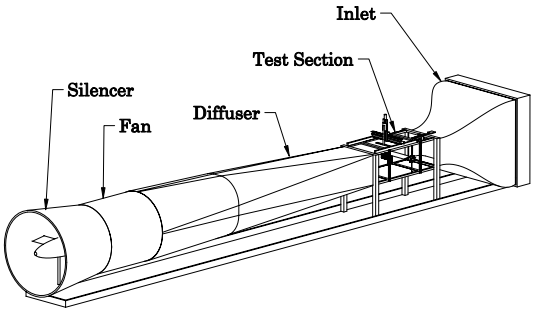

Figure 6: UIUC 3×4 ft low-speed subsonic wind tunnel.

Figure 8: Photograph of the UIUC 3×4 ft low-speed subsonic wind tunnel test section.

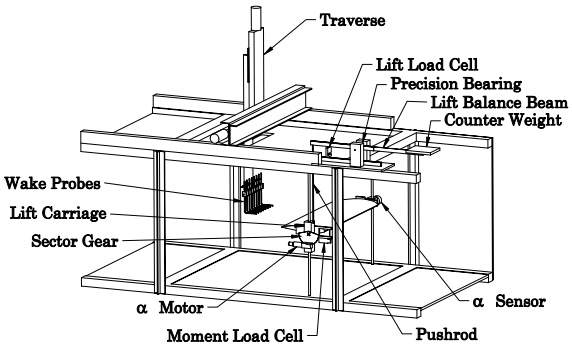

Figure 7: Experimental setup with Plexiglass splitter plates and traverse enclosure box not shown for clarity.

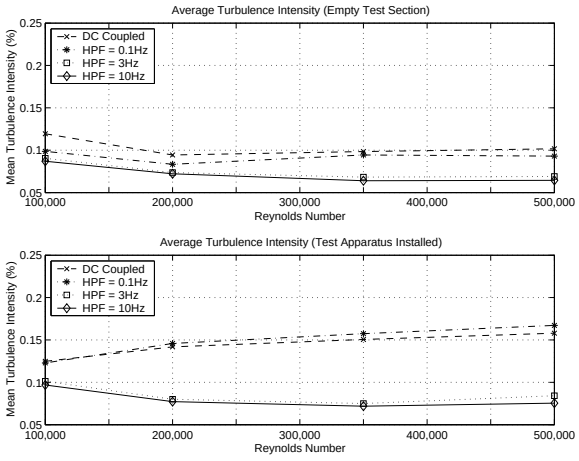

Figure 9: Turbulence intensity at tunnel centerline, empty test section and with rig in place.

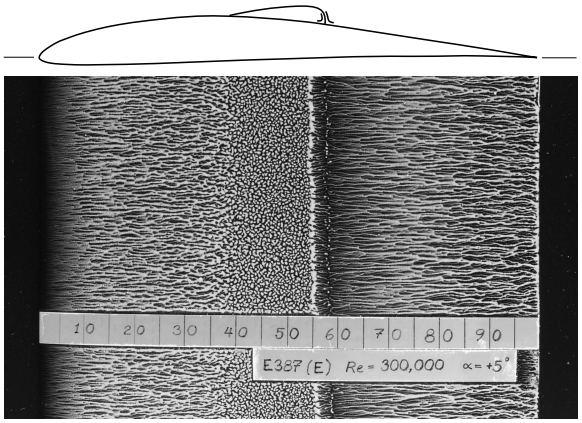

Figure 10: Representative upper-surface oil flow visualization on the E387, $\boldsymbol{Re} = 300{,}000$, $\alpha = 5$ deg.

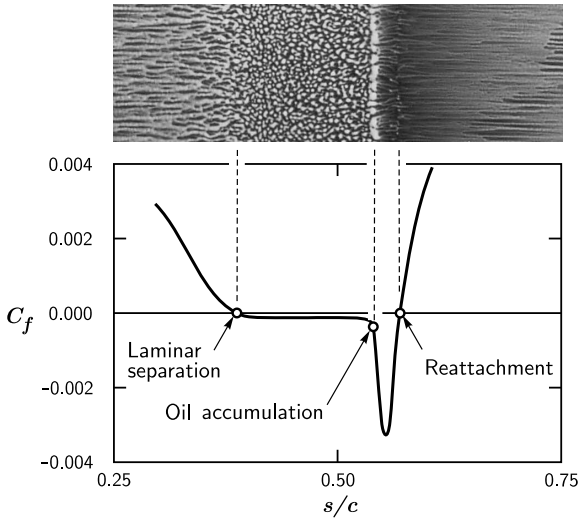

Figure 11: Conceptual illustration of the relationship between the surface oil flow features and skin friction distribution in the region of a laminar separation bubble plotted against the airfoil arc length.

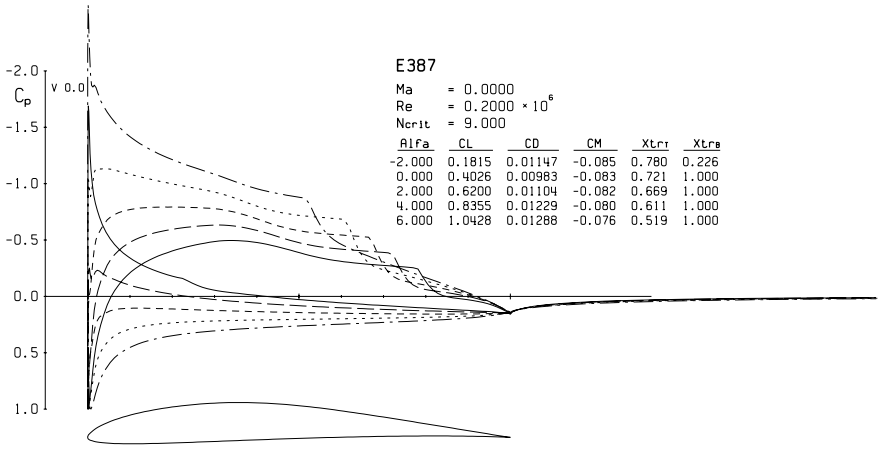

(a) $Re = 200{,}000$

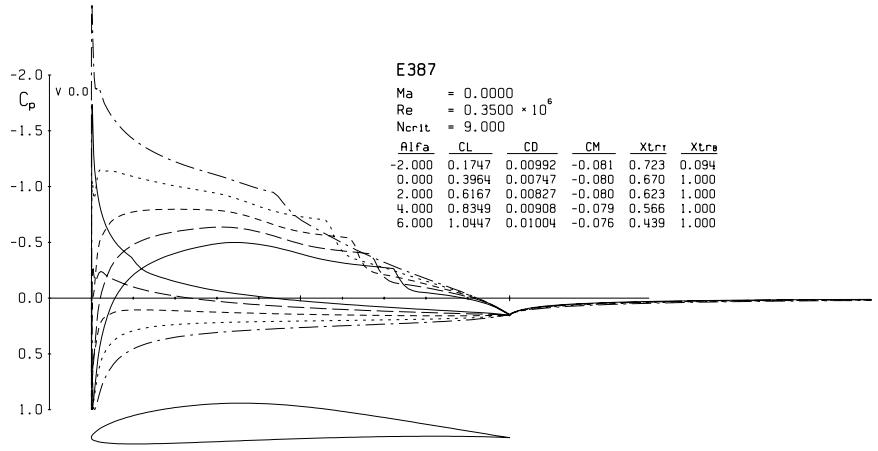

(b) $Re = 350{,}000$

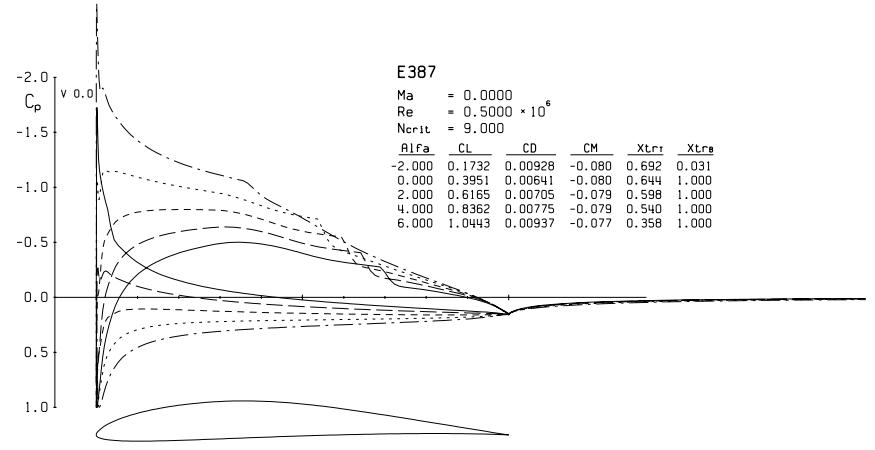

(c) $Re = 500{,}000$

Figure 12: Predicted pressure distributions and evidence of a laminar separation bubble on the E387 airfoil for several Reynolds numbers over a range of angles of attack.

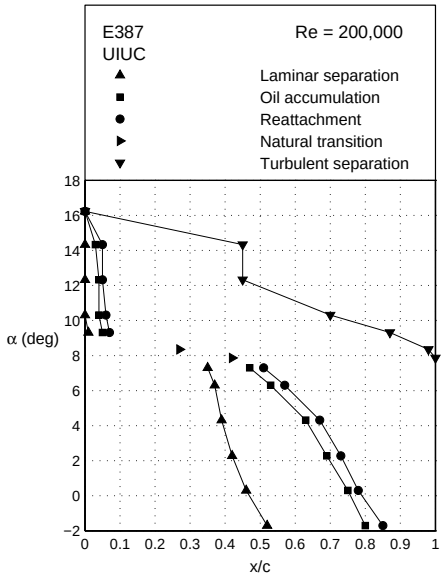

Figure 13: Locations of the upper surface flow features for the E387 airfoil at $\boldsymbol{Re} = 200{,}000$.

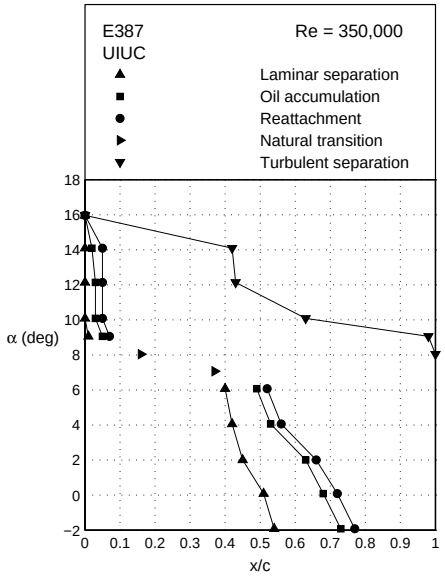

Figure 14: Locations of the upper surface flow features for the E387 airfoil at $\boldsymbol{Re} = 350{,}000$.

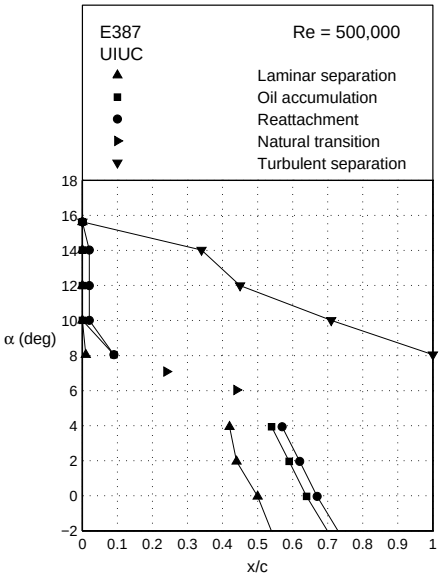

Figure 15: Locations of the upper surface flow features for the E387 airfoil at $\boldsymbol{Re} = 500{,}000$.

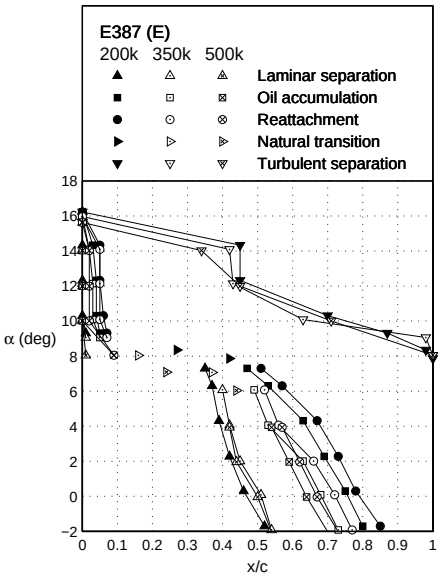

Figure 16: Locations of the upper surface flow features for the E387 airfoil for $\boldsymbol{Re} = 200{,}000$, 350,000 and 500,000 ('E' denotes that this is the 5th E387 model in the UIUC collection).

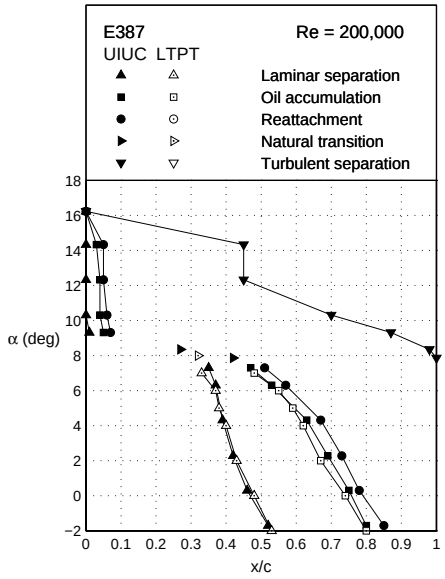

Figure 17: Comparison of major E387 upper-surface flow features between UIUC and NASA LTPT for $\boldsymbol{Re} = 200{,}000$.

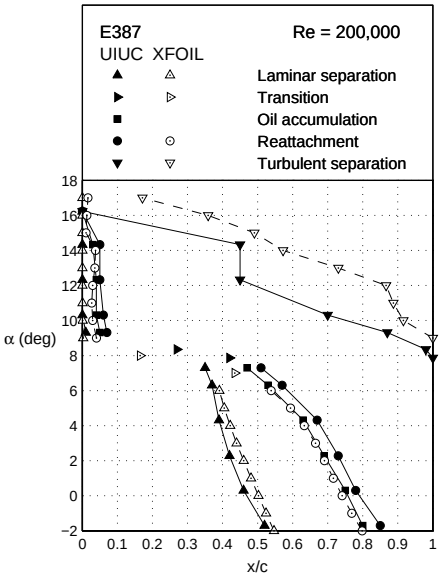

Figure 19: Comparison of major E387 upper-surface flow features between UIUC and XFOIL for $\boldsymbol{Re} = 200{,}000$.

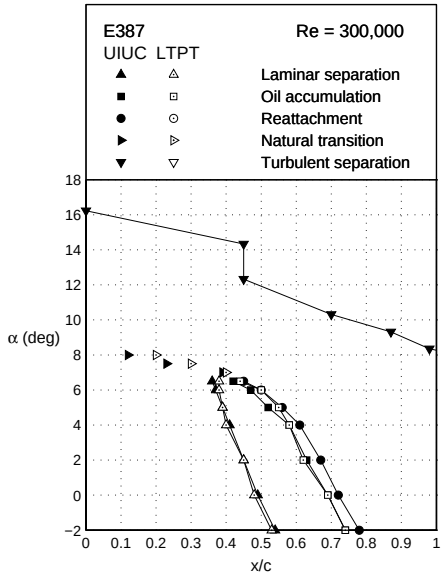

Figure 18: Comparison of major E387 upper-surface flow features between UIUC and NASA LTPT for $\boldsymbol{Re} = 300{,}000$.

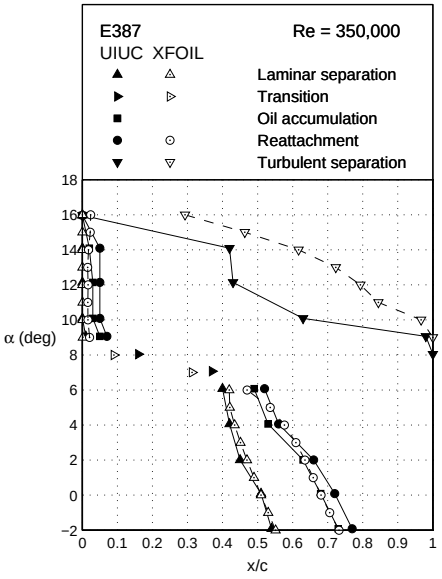

Figure 20: Comparison of major E387 upper-surface flow features between UIUC and XFOIL for $\boldsymbol{Re} = 350{,}000$.

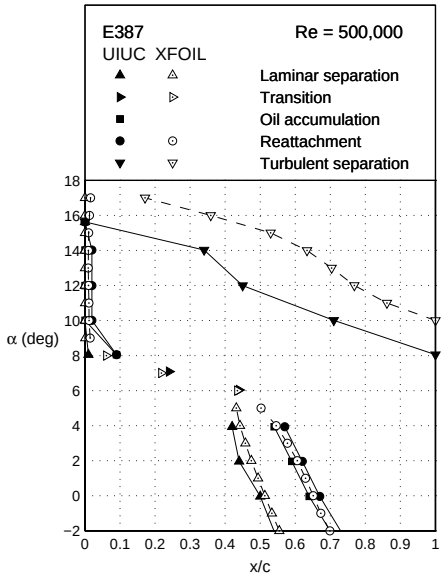

Figure 21: Comparison of major E387 upper-surface flow features between UIUC and XFOIL for $\boldsymbol{Re} = 500{,}000$.

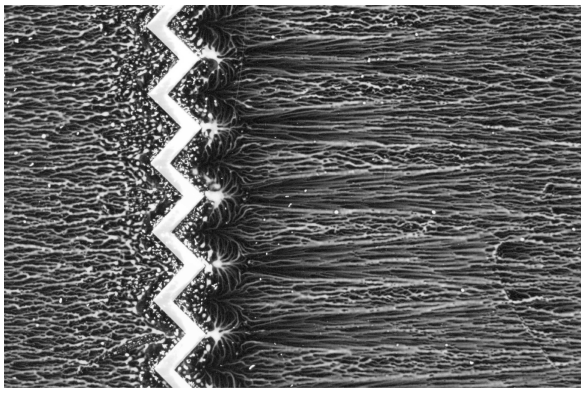

Figure 23: Surface oil-flow visualization on an airfoil with a zigzag boundary layer turbulator that promotes rapid transition at the trip location.

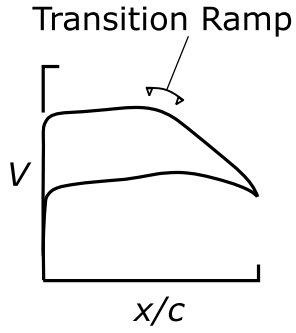

Figure 22: Conceptual illustration of a transition ramp on the upper surface of an airfoil.

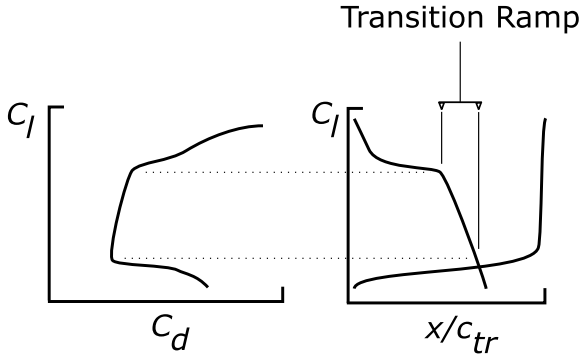

Figure 24: Defining the upper surface transition ramp as the chordwise extent over which transition moves while the airfoil operates in the low drag range of the polar.

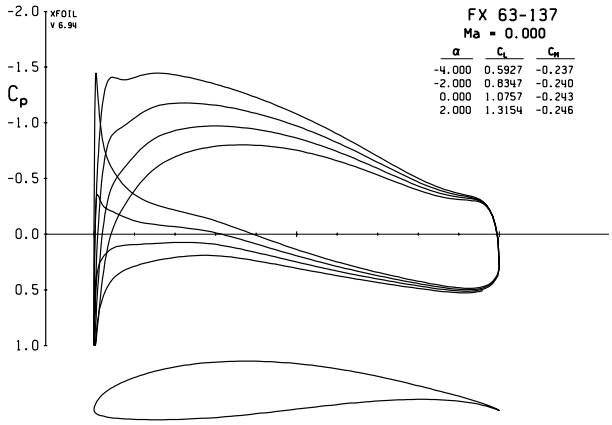

Figure 25: Inviscid pressure distributions for the FX 63-137 airfoil.

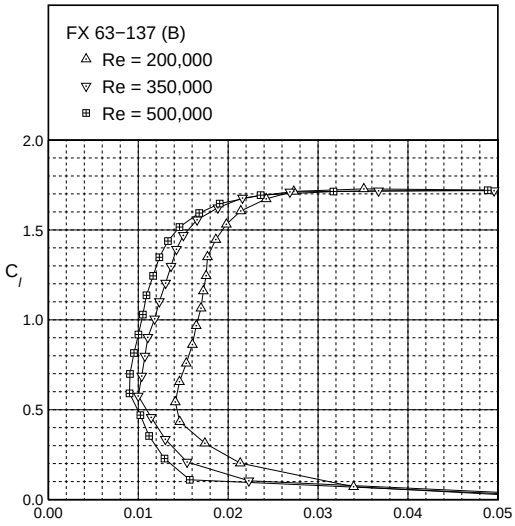

Figure 27: Measured performance for the FX 63-137.

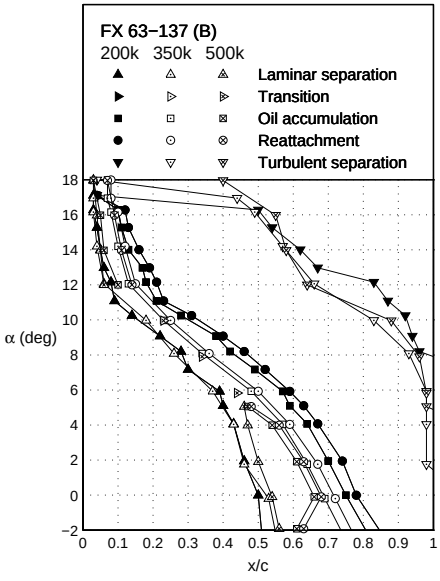

Figure 26: Locations of the upper surface flow features for the FX 63-137 airfoil for $\boldsymbol{Re}$ = 200,000, 350,000 and 500,000.

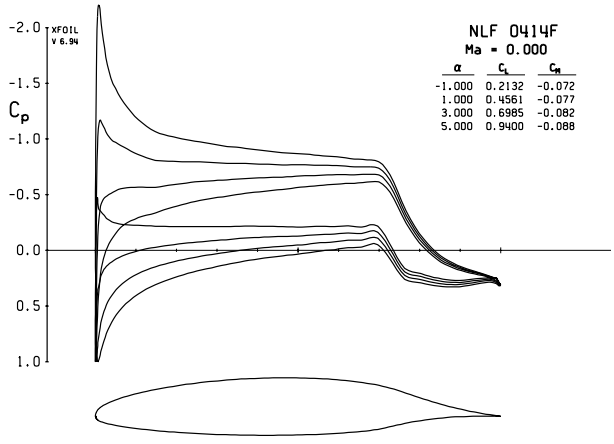

Figure 28: Inviscid pressure distributions for the NASA NLF(1)-0414F airfoil.

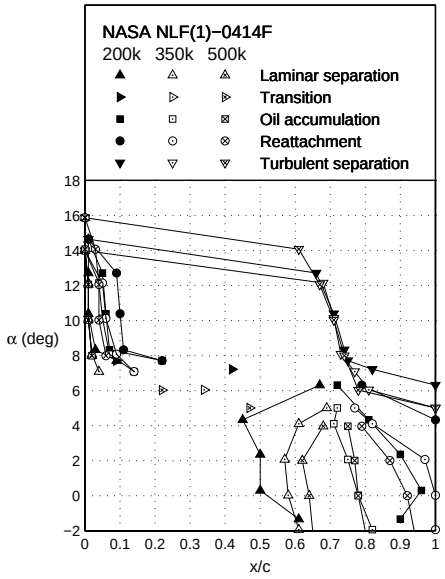

Figure 29: Locations of the upper surface flow features for the NASA NLF(1)-0414F airfoil for $\boldsymbol{Re} = 200{,}000$, 350,000 and 500,000.

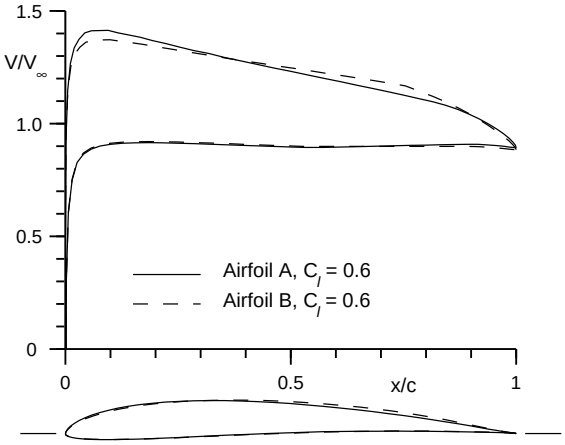

Figure 31: Inviscid velocity distributions for airfoils A and B to study the different effects on drag.

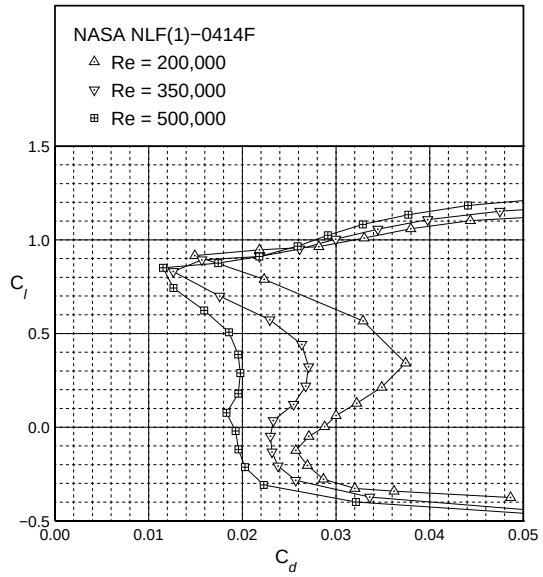

Figure 30: Measured performance for the NASA NLF(1)-0414F.

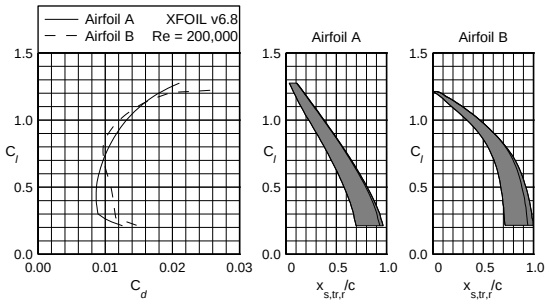

Figure 32: XFOIL predictions for airfoils A and B to illustrate the effects of changes in the transition ramp on drag.

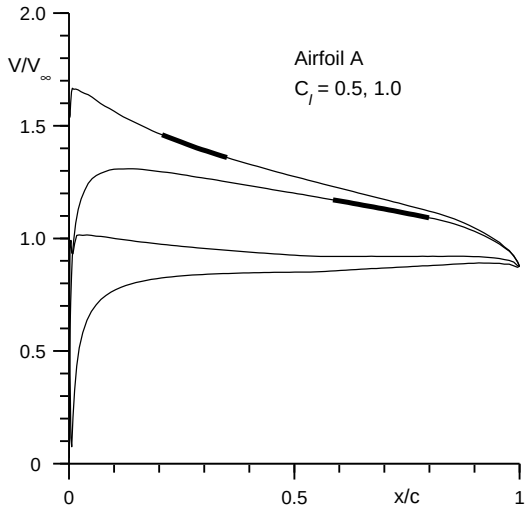

Figure 33: Inviscid velocity distributions for airfoil A with the locations of the bubble marked.

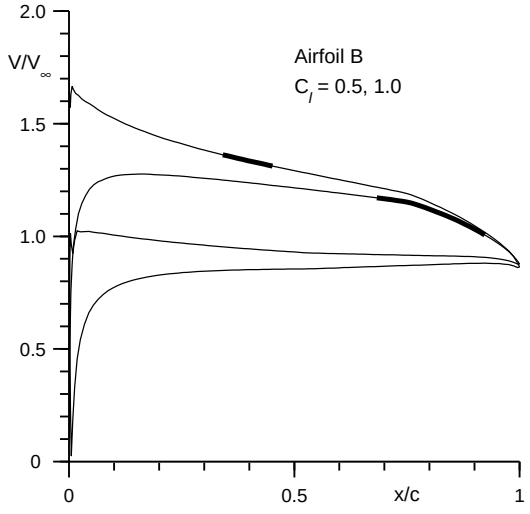

Figure 34: Inviscid velocity distributions for airfoil B with the locations of the bubble marked.

$$z = \zeta + c_0 + \frac{c_1}{\zeta} + \frac{c_2}{\zeta^2} + \cdots$$

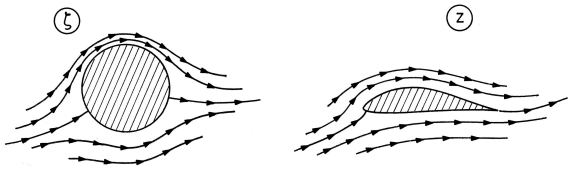

Figure 35: Conformal mapping of a circle to an airfoil.

Figure 36: Definitions of flow speed and angle on the airfoil.

1. Specify V subject to constraints
2. Find flow direction θ and V to form dF/dz

$$\frac{dF}{dz} = Ve^{-i\theta} \quad \Leftarrow \text{complex velocity on the airfoil}$$

$$\ln \frac{dF}{dz} = \ln V - i\theta$$

3. Find $dz/d\xi$

$$\frac{dz}{d\xi} = \frac{dF/d\xi}{dF/dz} \quad \begin{array}{l} \Leftarrow \text{complex velocity on circle (known)} \\ \Leftarrow \text{known from step 2} \end{array}$$

4. Integrate $dz/d\xi$ to get mapping

$$z = \int \frac{dz}{d\xi} d\xi$$

5. Obtain coordinates from the mapping

Figure 37: Flowchart of steps taken to obtain the geometry of an airfoil given the specified flow velocity (several details omitted).

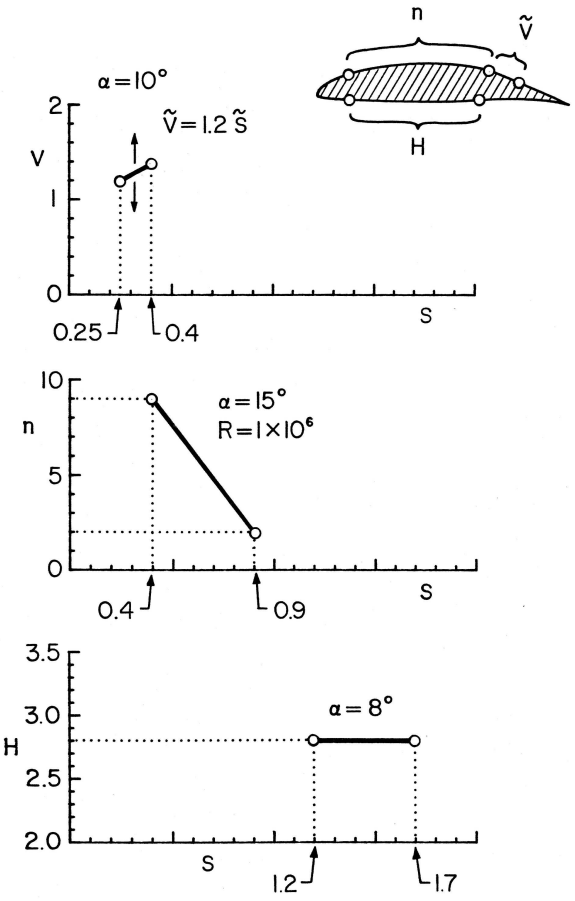

Figure 38: Specification to be achieved.

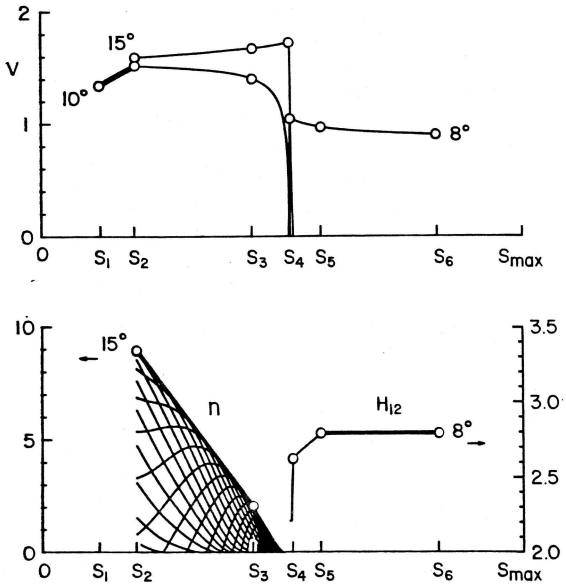

Figure 39: Partial velocity distributions and boundary-layer developments corresponding to the design conditions ($R = 1 \times 10^6$ for the n-development, $s_{max} = 2.067$).

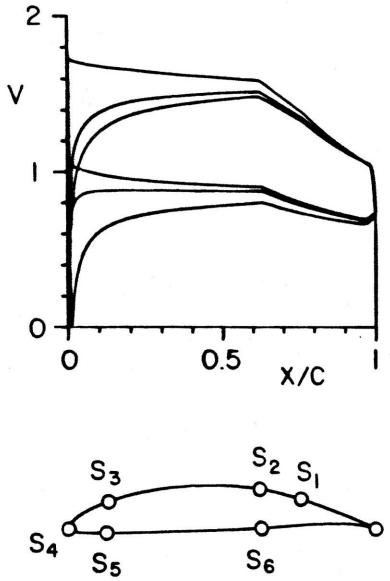

Figure 40: Airfoil and velocity distributions for $\alpha = 8$, 10 and 15 deg.

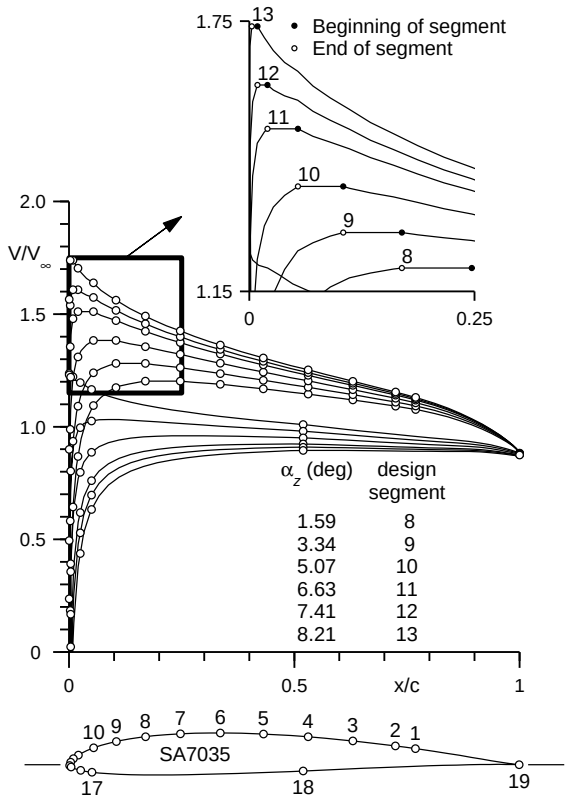

Figure 41: SA7035 inviscid velocity distributions showing the zero pressure-gradient segments and corresponding design angles of attack α^*.

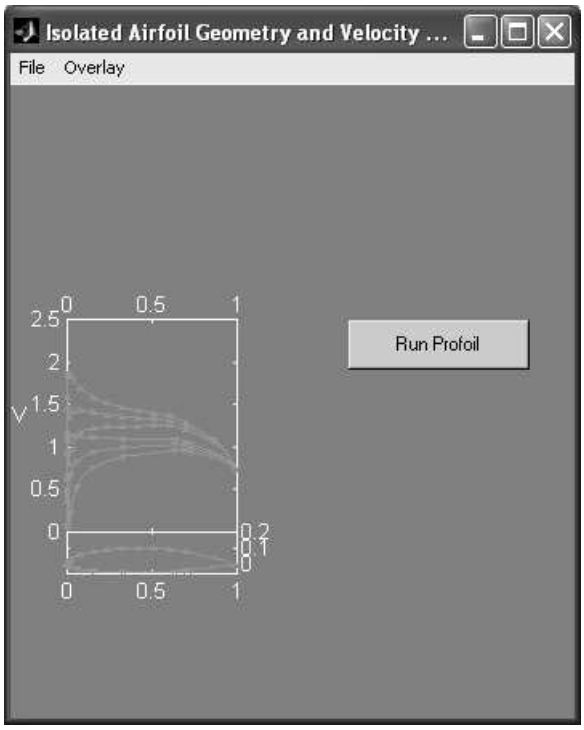

Figure 43: Interactive Matlab MFOIL GUI for PROFOIL showing the velocity distribution.

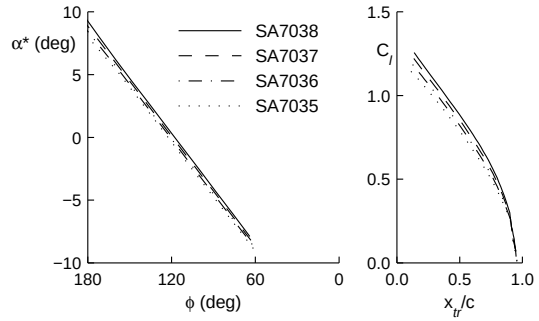

Figure 42: Linkage between the α^*-ϕ and C_l-x_{tr} curves for the SA703x airfoil series.

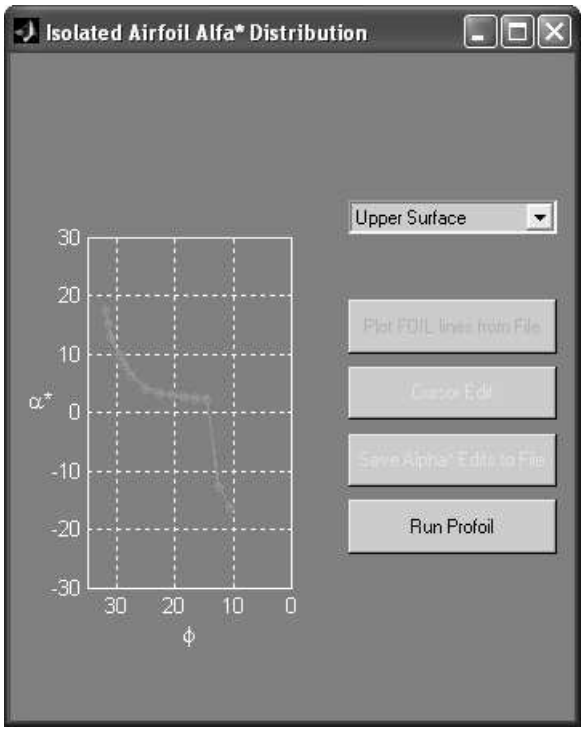

Figure 44: Interactive Matlab MFOIL GUI for PROFOIL showing the α^*-ϕ curve edit window.

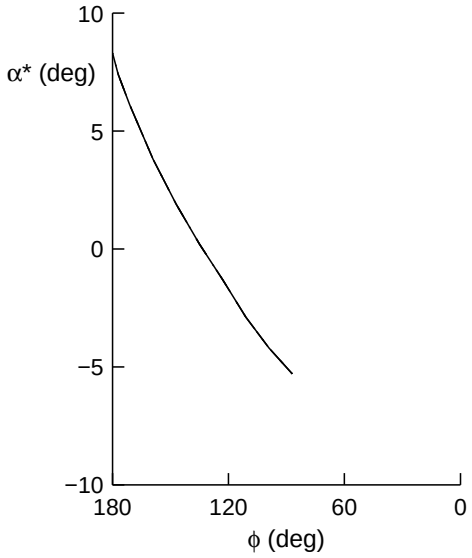

Figure 46: SD7003 airfoil α^*-ϕ curves for control over the C_l-x_{tr} curves.

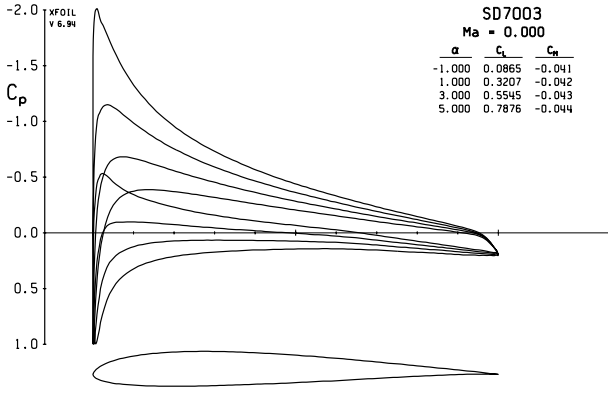

Figure 45: Inviscid pressure distributions for the SD7003 airfoil.

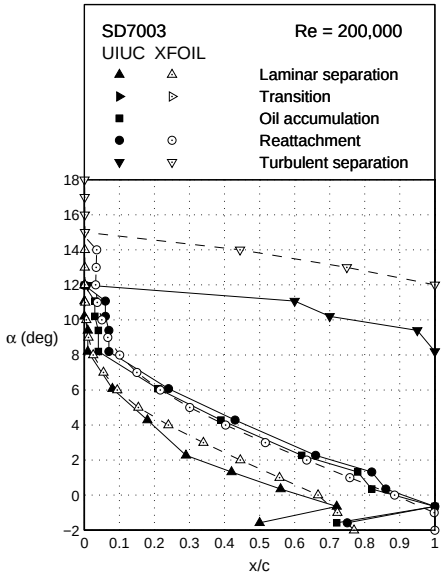

Figure 47: Comparison of major SD7003 upper-surface flow features between UIUC and XFOIL for $\boldsymbol{Re} = 200{,}000$.

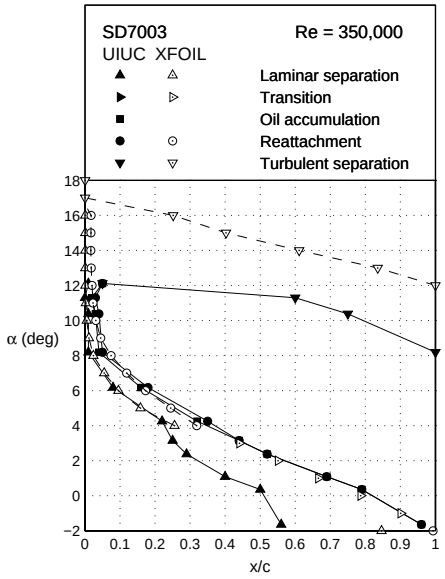

Figure 48: Comparison of major E387 upper-surface flow features between UIUC and XFOIL for $\boldsymbol{Re} = 350{,}000$.

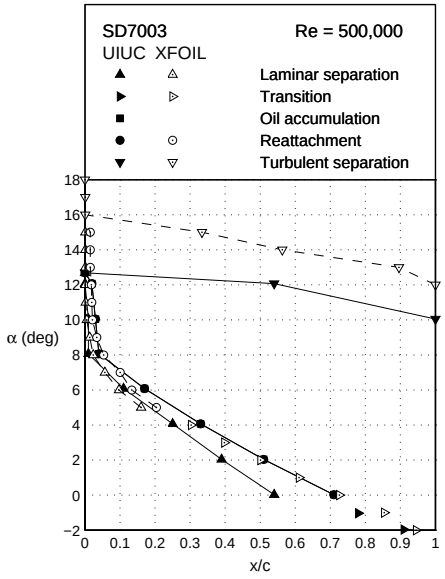

Figure 49: Comparison of major E387 upper-surface flow features between UIUC and XFOIL for $\boldsymbol{Re} = 500{,}000$.

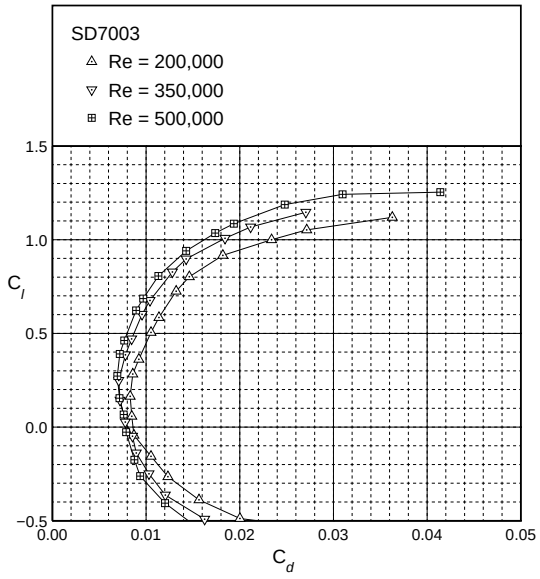

Figure 50: Measured performance for the SD7003.

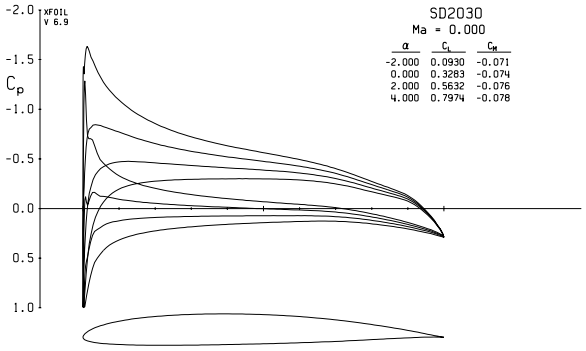

Figure 51: Inviscid pressure distributions for the SD2030 airfoil.

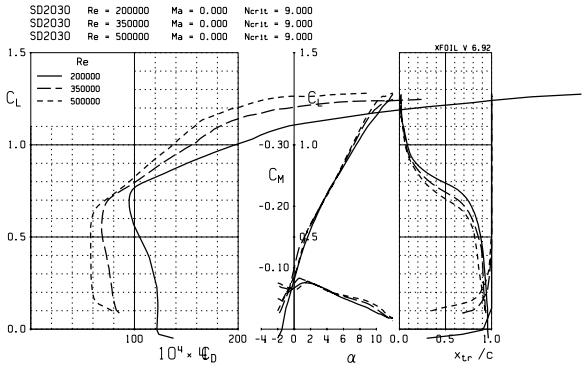

Figure 52: XFOIL predictions for the SD2030.

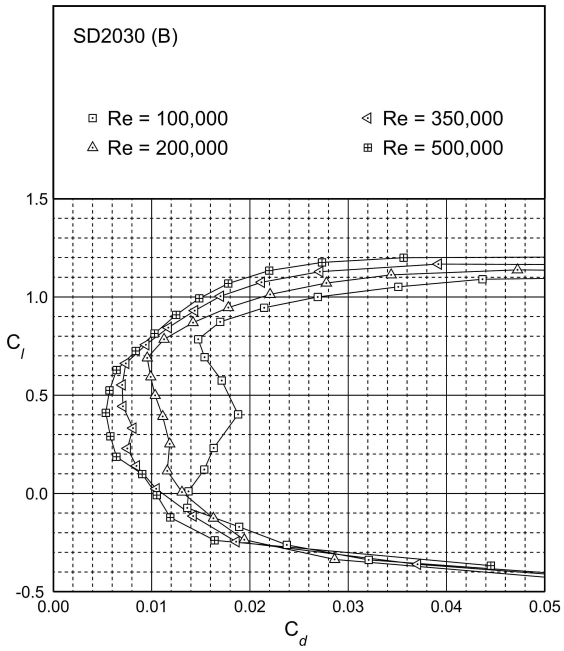

Figure 53: Measured performance for the SD2030.

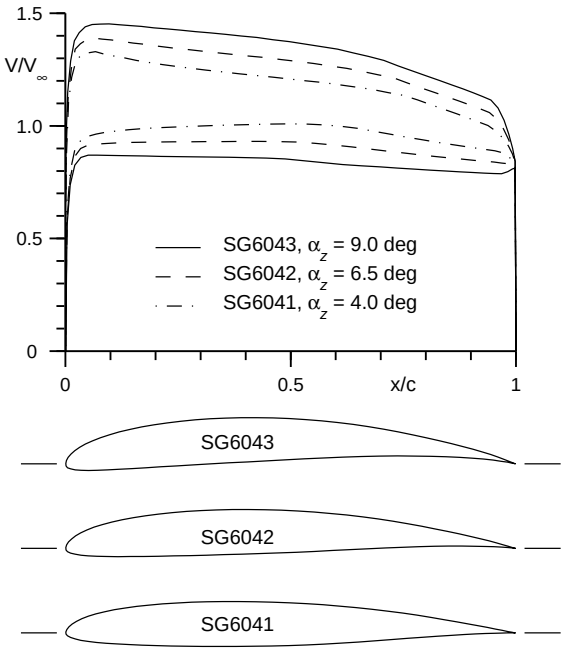

Figure 55: SG604x airfoils and inviscid velocity distributions.

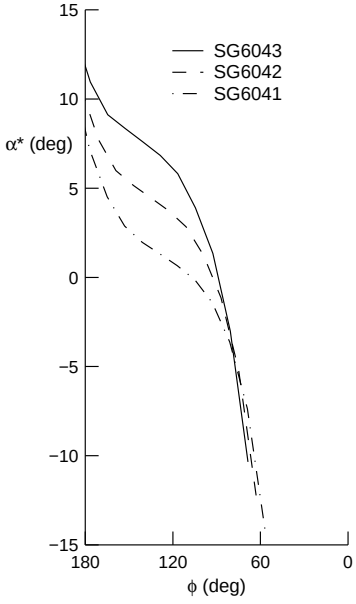

Figure 54: SG604x airfoil series α^*-ϕ curves for control over the C_l-x_{tr} curves.

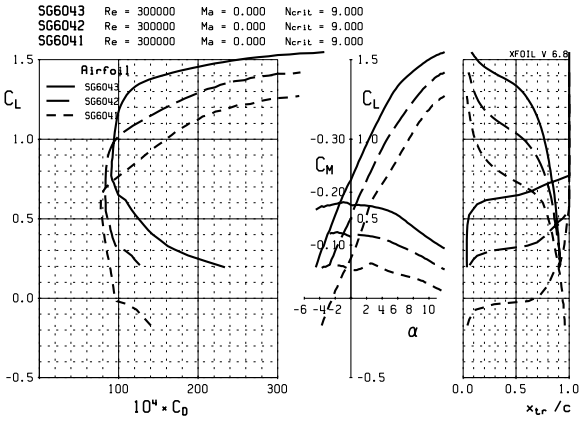

Figure 56: XFOIL predictions for the SG604x airfoil series.

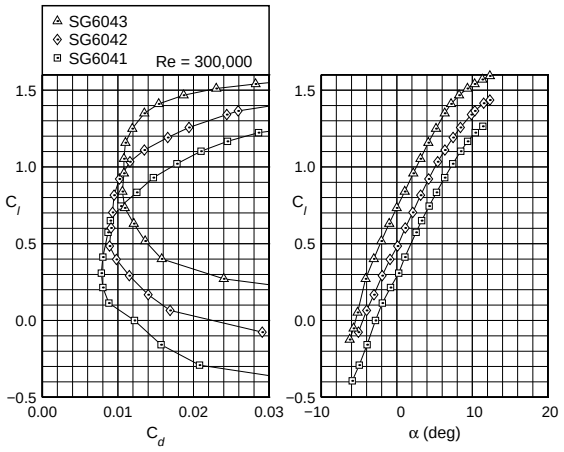

Figure 57: Measured performance for the SG604x airfoil series.

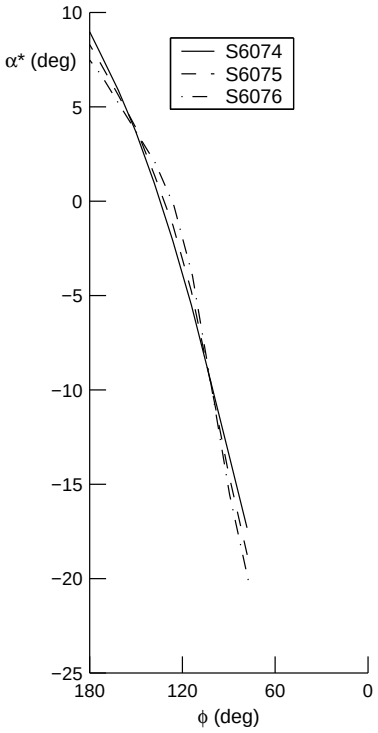

Figure 59: S6074/5/6 airfoil series α^*-ϕ curves for control over the C_l-x_{tr} curves.

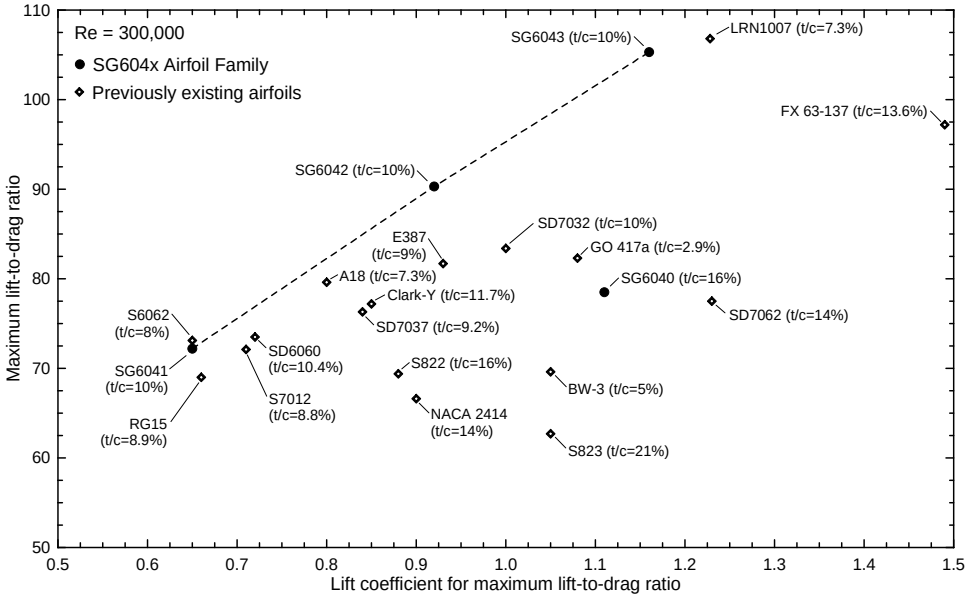

Figure 58: Maximum lift-to-drag ratio versus the corresponding lift coefficient for the SG604x airfoil series as compared with several previously existing airfoils.

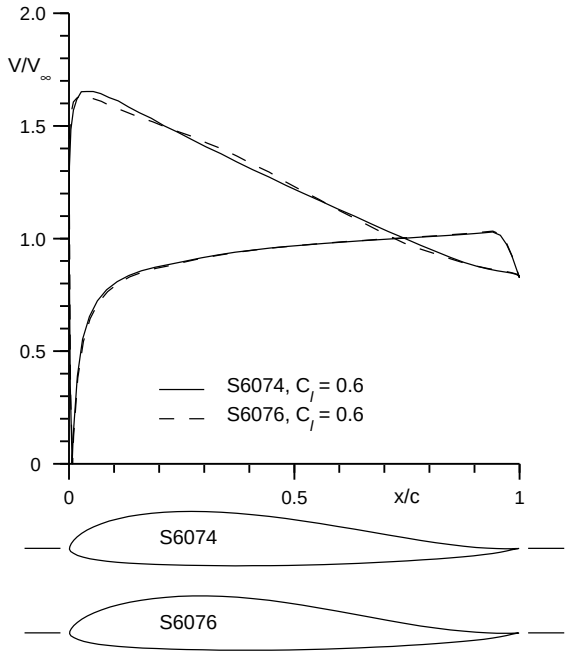

Figure 60: S6074/6 airfoils and inviscid velocity distributions.

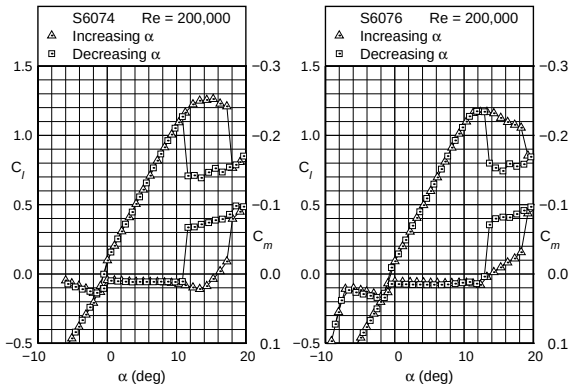

Figure 62: Measured lift curves for the S6074/6 airfoils.

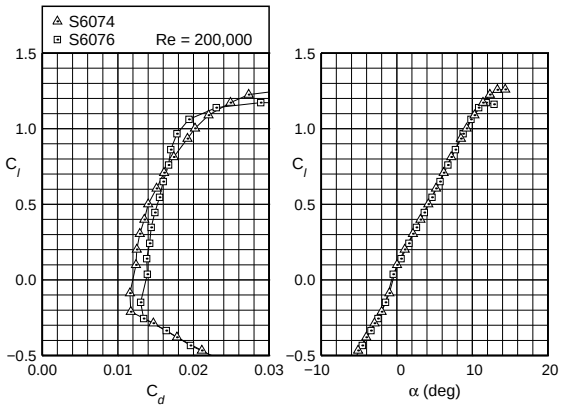

Figure 61: Measured drag polars for the S6074/6 airfoils.

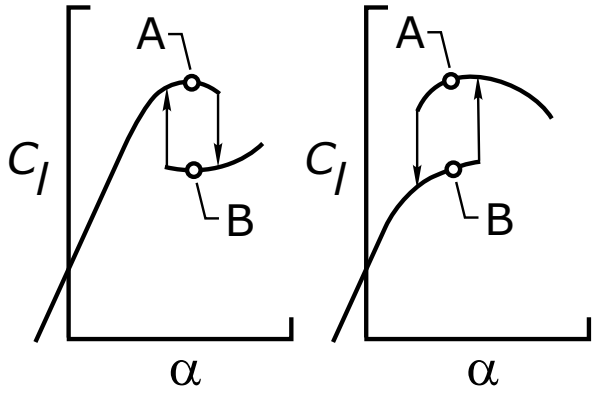

(a) Clockwise hysteresis loop

(b) Counter clockwise hysteresis loop

Figure 63: Two types of hysteresis in lift on airfoils at low Reynolds numbers.

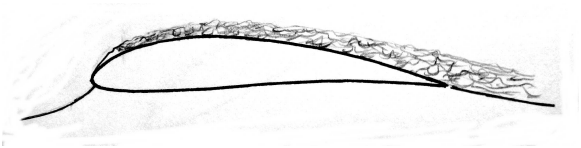

(a) Flow state A

(b) Flow state B

Figure 64: Flow states corresponding to the upper and lower branches of the hysteresis loops see in Fig. 63.

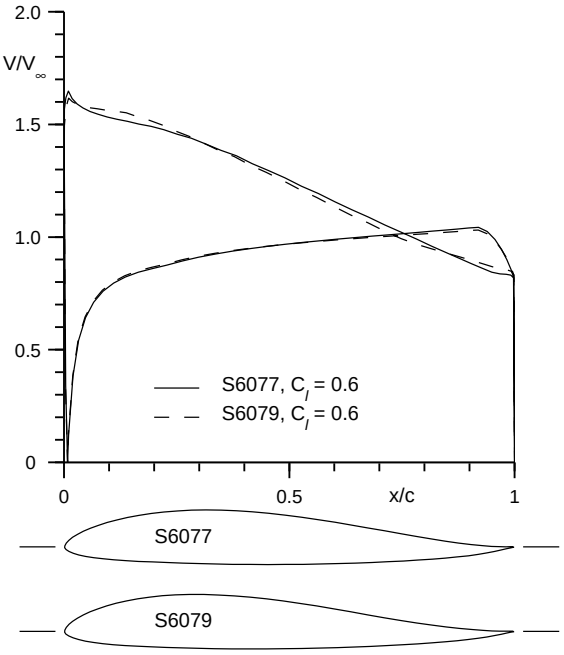

Figure 65: S6077/9 airfoils and inviscid velocity distributions.

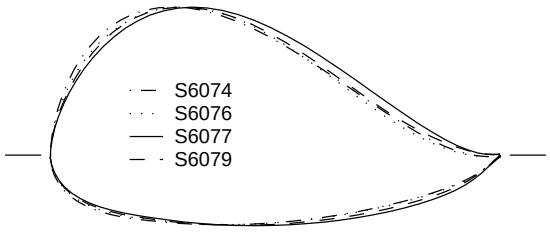

Figure 66: S6074/6/7/9 airfoils with the thickness magnified to show the small differences.

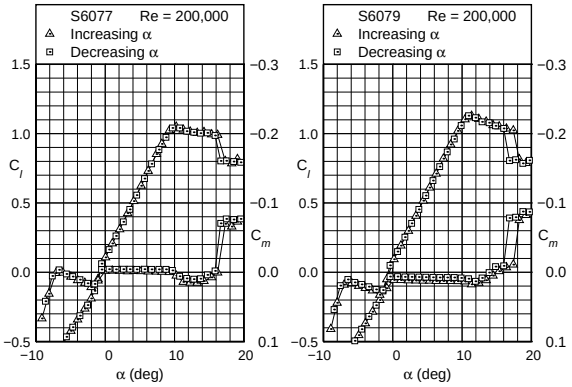

Figure 67: Measured lift curves for the S6077/9 airfoils.

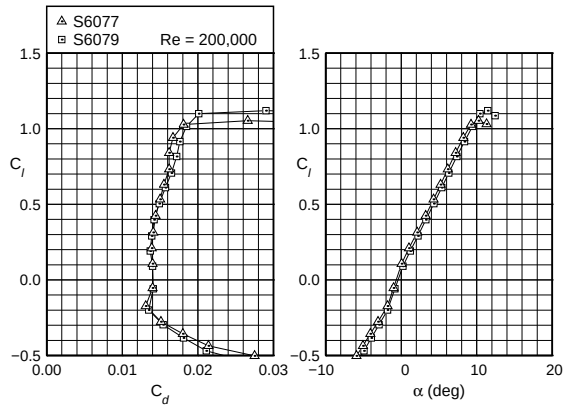

Figure 68: Measured drag polars for the S6077/9 airfoils.

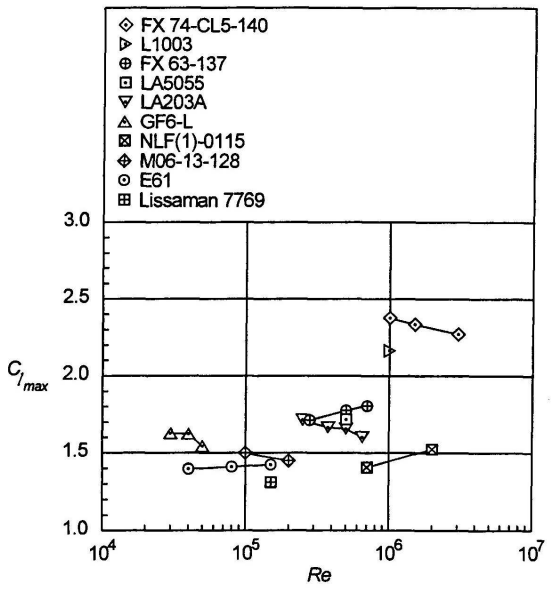

Figure 69: Maximum lift coefficient of several airfoils over a range of Reynolds numbers.

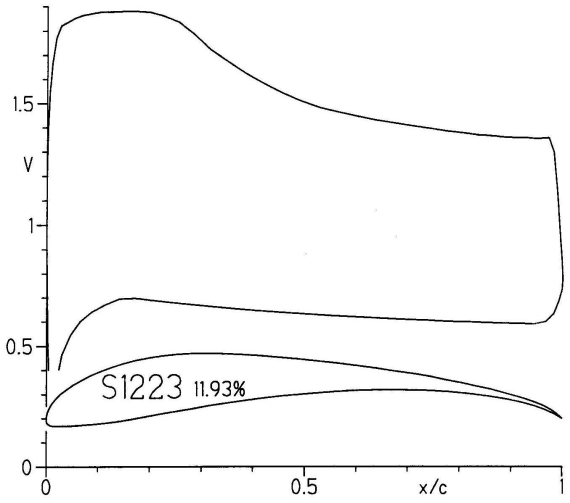

Figure 71: Inviscid velocity distributions for the S1223 airfoil for $C_l = 1.95$ (inviscid).

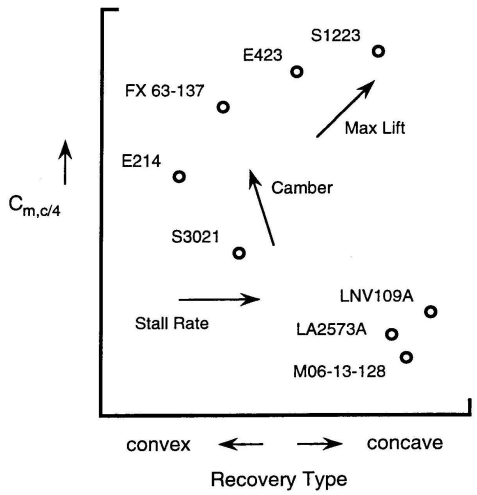

Figure 70: Trends in low Reynolds number airfoil characteristics as functions of the pitching moment and type of upper-surface pressure recovery distributions.

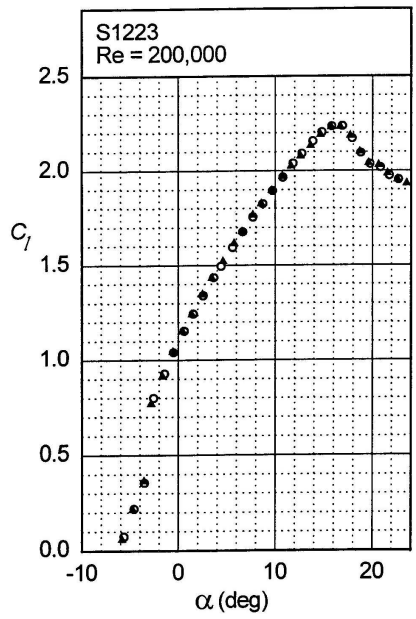

Figure 72: Measured lift characteristics for the S1223 airfoils at $\boldsymbol{Re} = 200{,}000$.

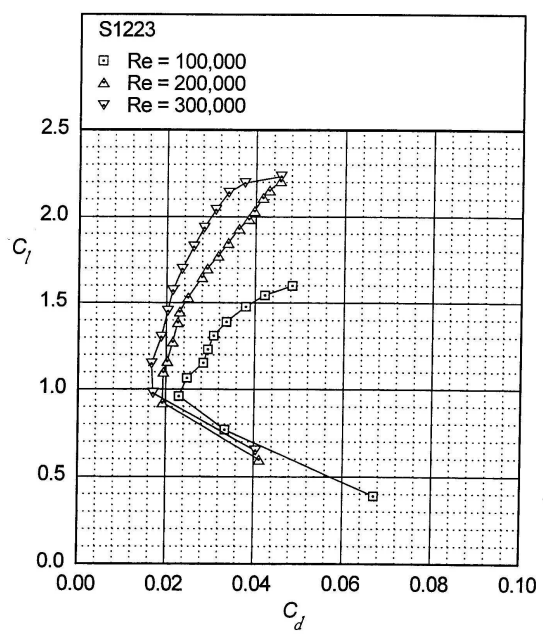

Figure 73: Measured performance for the S1223.

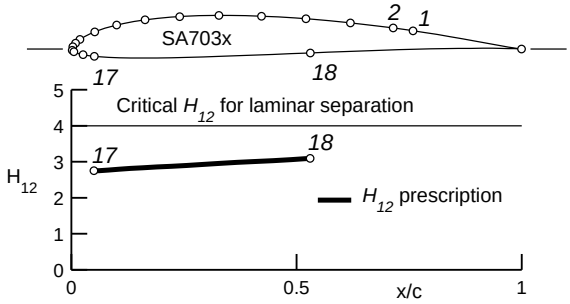

Figure 75: Lower-surface laminar boundary-layer development prescribed for the SA703x airfoil series for the lower corner of the drag polar.

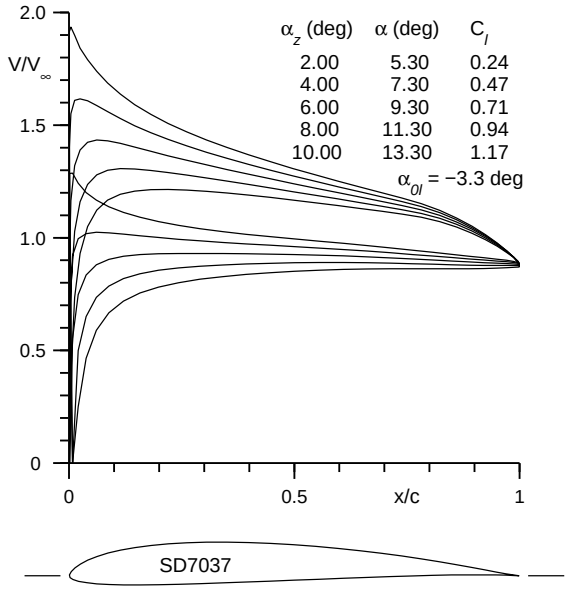

Figure 74: SD7037 airfoil and inviscid velocity distributions.

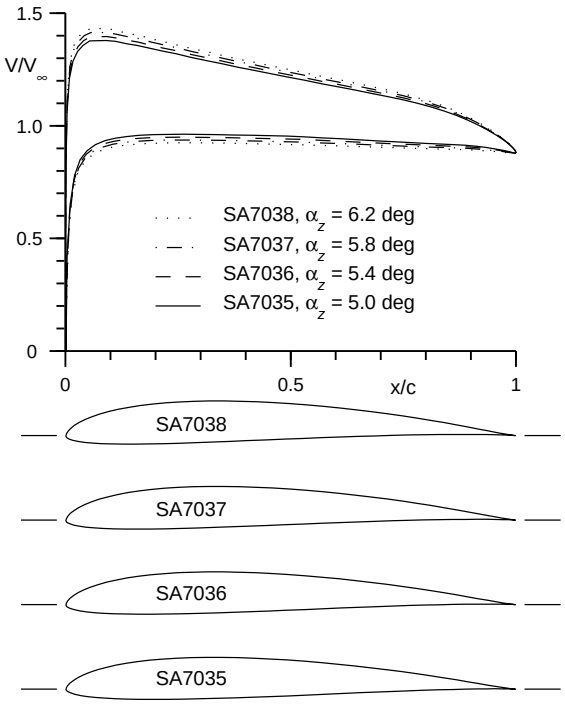

Figure 76: SA703x airfoils and inviscid velocity distributions.

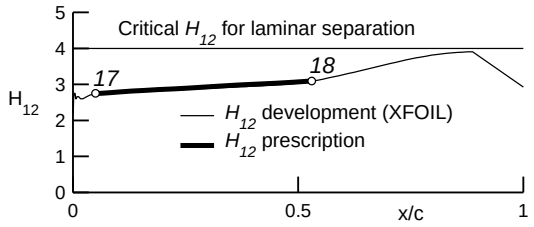

Figure 77: Laminar boundary-layer development achieved for the SA703x airfoils and the agreement with the prescription.

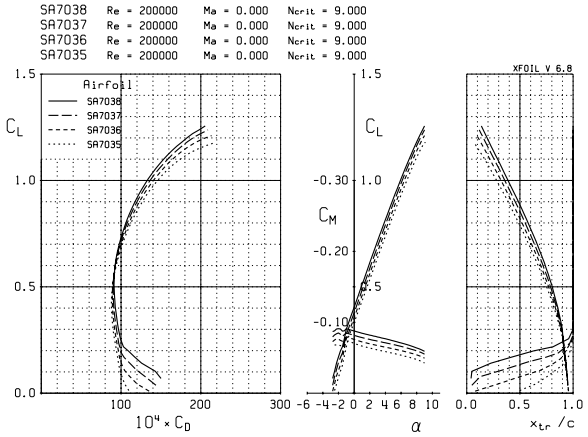

Figure 78: XFOIL predictions for the SA703x airfoil series.

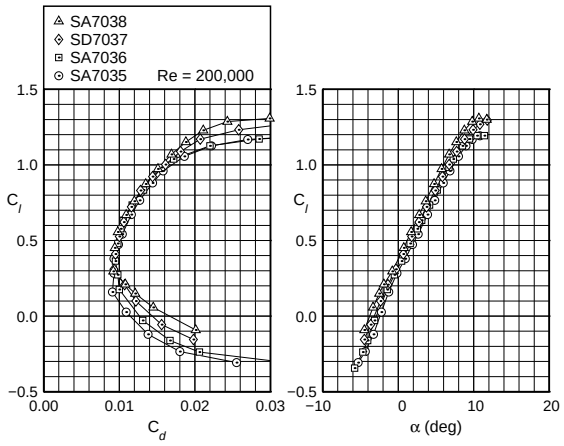

Figure 79: Measured performance for the SA703x airfoil series.